HHS Public Access

Author manuscript

Methods Mol Biol. Author manuscript; available in PMC 2017 March 13.

Published in final edited form as:

Methods Mol Biol. 2009 ; 489: 317–357. doi:10.1007/978-1-59745-543-5_15.

Advanced In Vivo Heteronuclear MRS Approaches for Studying Brain Bioenergetics Driven by Mitochondria

Xiao-Hong Zhu, **Fei Du**, **Nanyin Zhang**, **Yi Zhang**, **Hao Lei**, **Xiaoliang Zhang**, **Hongyan Qiao**, **Kamil Ugurbil**, and **Wei Chen**

Abstract

The greatest merit of in vivo magnetic resonance spectroscopy (MRS) methodology used in biomedical research is its ability for noninvasively measuring a variety of metabolites inside a living organ. It, therefore, provides an invaluable tool for determining metabolites, chemical reaction rates and bioenergetics, as well as their dynamic changes in the human and animal. The capability of in vivo MRS is further enhanced at higher magnetic fields because of significant gain in detection sensitivity and improvement in the spectral resolution. Recent progress of in vivo MRS technology has further demonstrated its great potential in many biomedical research areas, particularly in brain research. Here, we provide a review of new developments for in vivo heteronuclear ^{31}P and ^{17}O MRS approaches and their applications in determining the cerebral metabolic rates of oxygen and ATP inside the mitochondria, in both animal and human brains.

Keywords

In vivo ^{31}P MRS; in vivo ^{17}O MRS; in vivo heteronuclear MRS; brain; magnetic field; cerebral bioenergetics; brain metabolism; brain function; MRI

1. Introduction

1.1. Cerebral Bioenergetics and Brain Function

The brain is an extraordinary organ; with its unique structure and complex functions, it distinguishes itself from other organs in many aspects. Unlike cardiac and skeletal muscles, the brain does not perform mechanical work. The major cellular functions in the brain include excitation and conduction resulting in unceasing electrophysiological activities in normal brain, even at rest. These integrated neuronal activities are essential for performing brain functions. Nevertheless, to sustain these activities and functionalities, the brain has a high energy demand which is mainly fulfilled by the energy metabolism at the cellular level through adenosine triphosphate (ATP) production and utilization (1–8).

The vast majority of ATP formation relies on the oxidative phosphorylation occurring inside the mitochondria. The activity of cytochrome oxidase, a key mitochondrial enzyme of oxidative energy metabolism, is regulated by the cell functional activities and their energy demand (9, 10). At normal condition, the cerebral oxidative phosphorylation is expected to be tightly coupled and supported by the oxygen metabolism.

Figure 15.1 illustrates a simplified schema showing the major metabolic processes and ATP energy transportation occurring at various subcellular compartments and the associated hemodynamic processes for supporting normal brain function. Oxygen and glucose are the major chemical substrates for brain metabolism and they are continuously supplied by the circulating blood in the capillary bed. Glucose is first converted to two pyruvate molecules in the cytosol, then the pyruvate enters the mitochondria and is metabolized oxidatively with diffused oxygen molecules through the mitochondrial respiratory chain and the cytochrome oxidase enzyme resulting in substantial oxygen utilization and final products of water and CO_2 (i.e., Reaction 1 or **R1** in Fig. 15.1). This oxygen metabolism is coupled with the oxidative phosphorylation for producing ATP from inorganic phosphate (Pi) and adenosine diphosphate (ADP) through the enzyme of F_1F_0-ATP_{ase} inside the mitochondria (i.e., Reaction 2 or **R2** in Fig. 15.1). In general, the mitochondrial oxidative phosphorylation dominates up to 90% of ATP production (11). In contrast, ATP utilization mainly occurs in the cytosol space resulting in ADP and Pi products (i.e., Reaction 5 or **R5** in Fig. 15.1), ultimately, providing chemical energy for supporting various cellular activities and brain functions, in which a significant amount of ATP energy is used for neuronal signaling. This ATP utilization is particularly essential for maintaining and restoring the Na^+/K^+ ion gradients across the cellular membranes through the enzyme of Na^+/K^+-ATP_{ase} as well as for supporting the signaling process (e.g., neuronal transmission and cycling) at resting and activated brain states (11–14).

The high energy demand in the brain causes extremely fast chemical cycling among ATP, ADP and Pi, which requires rapid transportation of these phosphate components between the cytosolic and mitochondrial compartments. This energy transportation could be partially accomplished by phosphocreatine (PCr) through the reversible creatine kinase (CK) reaction, thus, maintaining a stable ATP level in the brain cells (15–17). There are at least two apparently coupled CK reactions: one occurring in the mitochondrial intermembrane space (i.e., Reaction 3 or **R3** in Fig. 15.1) and another one occurring in the cytosol space (i.e., Reaction 4 or **R4** in Fig. 15.1) although, in reality, these coupled CK reactions likely exist of these subcellular spaces. They play an important role in carrying the ATP molecules generated in the mitochondria into the cytosol for energy utilization, and then to bring the products of ADP and Pi back to mitochondria for sustaining ATP production. Therefore, PCr serves a vital role for energy transportation among subcellular compartments. Four ATP-related reactions (two reactions each for ATP_{ase} and CK) constitute a complex ATP metabolic process. They are tightly coupled and integrated with the oxygen metabolism and the hemodynamic process as depicted in Figure 15.1 for controlling the dynamics of ATP production and utilization, all of which play a central role in the cerebral bioenergetics and function in normal and diseased brains. Development of in vivo tools being able to noninvasively detect and quantify the cerebral metabolic rate of oxygen utilization ($CMRO_2$) and ATP formation (CMR_{ATP}), therefore, become extremely important for studying and understanding the relation between ATP metabolism and cerebral bioenergetics and its impact on brain function.

1.2. In Vivo Heteronuclear MRS Approaches for Studying Brain Bioenergetics and Function

Although there are a number of techniques capable of studying brain metabolism, in vivo heteronuclear magnetic resonance spectroscopy (MRS) allows for noninvasively determining the physiological parameters and their changes that can be linked to brain metabolism, chemical kinetics and cerebral bioenergetics. The most commonly used in vivo heteronuclear MRS approaches for studying brain bioenergetics are in vivo ^{31}P, ^{13}C and ^{17}O MRS. Here, we will focus on ^{31}P and ^{17}O MRS in vivo.

In vivo ^{31}P MRS allows noninvasive assessment of numerous fundamental biochemical, physiological and metabolic events occurring inside a living brain (e.g., (17–23)). The primary information provided by in vivo ^{31}P MRS includes: intracellular pH, intracellular free magnesium concentration ([Mg^{2+}]) and high-energy phosphate (HEP) metabolites such as ATP, ADP and PCr. All these phosphate metabolites (except ADP) and Pi can be directly observed in an in vivo ^{31}P MR spectrum as demonstrated in Fig. 15.2A which was acquired from the human occipital-lobe at high field (7 tesla) (24). The pH value can be calculated from the chemical shift difference (δ_i) between the Pi and PCr resonance peaks according to the following equation: (25)

$$pH = 6.77 + log\left[\frac{\delta_i - 3.29}{5.68 - \delta_i}\right] \quad (15.1)$$

and [ADP] can be calculated by the following equation:

$$[ADP] = \frac{[ATP]\,([Cr] - [PCr])}{K_{eq}\,[PCr]\,[H^+]} \quad (15.2)$$

where K_{eq} is the equilibrium constant of the creatine kinase reaction and [Cr] is the total creatine concentration given by the summation of PCr and non-phosphorylated Cr.

Besides the aforementioned phosphate compounds and physiological parameters, other detectable phosphate compounds in the human brain ^{31}P MRS include: uridine diphospho (UDP) sugar (an important precursor for glycogen metabolism), diphospho nicotinamide adenine dinucleotides (NAD) involving oxidative respiratory chains, and four resolved phosphate compounds of glycerophosphoethanolamine (GPE), glycerophosphocholine (GPC), phosphoethanolamine (PE) and phosphocholine (PC), which are actively involved in the membrane phospholipid metabolism through phospholipid biosynthetic enzymes (26–29). In vivo ^{31}P MRS has been widely applied to study both normal and diseased brains and has led to a large number of publications (e.g., (19, 21–24, 26–28, 30–42). The abnormality in the HEP metabolites has been frequently observed in the diseased brains using in vivo ^{31}P MRS, and these changes or the change of HEP concentration ratios have been commonly applied in many clinical studies.

Although the steady-state concentrations of cellular HEP metabolites are closely linked to the ATP metabolism, they are relatively stable under normal physiological conditions. This

could be attributed to the rigorous regulation of the ATP metabolic reactions and their kinetics (see Fig. 15.1) for maintaining stable chemical energy supply of ATP in the brain. This is likely the case for the brain activation caused by brain stimulation and task performance. Thus, the measurements of the kinetics of ATP metabolism (i.e. reaction rate constants and fluxes) should logically be more sensitive and meaningful for quantifying the cerebral bioenergetics and its change under varied brain activity states as compared to the measurement of steady-state ATP concentrations. In vivo ^{31}P MRS, in combination with the magnetization transfer (MT) approach (18, 43–48), is capable of noninvasively determining the chemical reaction fluxes related to the ATP metabolism and enzyme activity; and thus becomes an important tool for studying the brain ATP metabolisms and cerebral bioenergetics. One example is to apply this approach for measuring the metabolic flux of oxidative phosphorylation in the brain (20,49,50). This useful in vivo approach and its new development will be described here.

Another alternative in vivo heteronuclear MRS approach which can directly and noninvasively assess the fluxes of oxidative metabolism occurring in the mitochondria (i.e., **R1** in Fig. 15.1) is the use of in vivo ^{17}O MRS approach for imaging $CMRO_2$ (e.g., (51–54) and a recent review article (55) and the references cited therein). The basic idea underlying this approach is to apply in vivo ^{17}O MRS for detecting the dynamic change of the ^{17}O-labeled metabolic water ($H_2\,^{17}O$) produced through the metabolism of inhaled $^{17}O_2$ gas, and ultimately for determining and imaging $CMRO_2$. Recent progress, especially at ultrahigh fields, has advanced the in vivo ^{17}O MRS methodology for imaging $CMRO_2$ and great promise has been demonstrated in the animal applications at high fields. This topic is also discussed here in some detail.

Although the metabolic fluxes measured by in vivo ^{31}P MRS and in vivo ^{17}O MRS reflect different metabolic reactions and pathways, these two MRS approaches are quite complementary. They are vital for investigating the coupling between the oxygen utilization and oxidative phosphorylation in the brain mitochondria under normal and pathological conditions.

2. Benefit of In Vivo ^{31}P and ^{17}O MRS at Ultrahigh Magnetic Field

2.1. Challenges of In Vivo Heteronuclear MRS

In practice, in vivo heteronuclear MRS faces many technical challenges due to its unfavorable sensitivity. For instance, the phosphate metabolites detected by in vivo ^{31}P MRS and the metabolic $H_2\,^{17}O$ detected by in vivo ^{17}O MRS are in a range of few millimolar concentrations, which are approximately 5000 times lower than the tissue water concentration, resulting in a much lower detection sensitivity. Thus, a high number of signal averaging is required to achieve reasonable spectral quality. This low sensitivity is even more manifest for the nuclear spins (e.g., ^{31}P and ^{17}O) with a relatively low magnetogyric ratio (γ) compared to in vivo ^{1}H MRS. This significantly limits the reliability, applicability, spatial and temporal resolutions of in vivo ^{31}P and ^{17}O MRS for general application, as well as clinical studies. One common trade off is to reduce the spatial and/or temporal resolution of in vivo MRS, thereby gaining detection sensitivity. However, in order to determine the nonuniform distribution of cerebral metabolites and chemical reaction fluxes in different

brain regions, there is a high demand on improving the spatial resolution of in vivo MRS. Moreover, the dynamic changes caused by physiological perturbation (e.g., sensory stimulation) may occur in a relatively short time and the magnitudes of the changes are usually subtle compared to those observed under pathological states. Therefore, both reasonably high spatial and temporal resolutions are desired and they rely heavily on the achievable detection sensitivity, which poses the major challenge for in vivo heteronuclear MRS. One way to overcome this challenge is the use of high/ultrahigh field MRS. Besides the sensitivity gain at high fields, the spectral resolution of in vivo MRS is also significantly improved and many overlapped resonance peaks from different metabolites as observed at low fields become resolvable at ultrahigh fields as demonstrated in Fig. 15.2A.

2.2. Sensitivity Improvement of In Vivo Heteronuclear MRS at High Field

One of the most important advantages at ultrahigh fields is the potential gain in detection sensitivity. This is particularly crucial for the low γ nuclei MRS such as in vivo ^{17}O and ^{31}P MRS. However, it is not so straightforward to evaluate and compare detection sensitivity (or signal-to-noise ratio, SNR) at different magnetic field strengths (B_0). The apparent SNR achievable at a given field strength relies not only on the B_0 but also on other B_0-dependent parameters, such as the longitudinal relaxation time (T_1), the apparent transverse relaxation time (T_2*) and the repetition time (TR) for acquiring MRS signal. It is, in general, more useful to determine and evaluate the SNR of signal detected in a given unit sampling time under optimal acquisition condition, which means that the excitation flip angle (a) satisfies the Ernst equation of $\cos(\alpha_{opt}) = \exp(-TR/T_1)$ (56). For a simple case with the single pulse and data acquisition scheme, such an averaged SNR can be quantified by Eq. (15.3) (56–60),

$$SNR\,(\text{per unit sampling time}) \propto C_\gamma{}^{2.5} B_0^\beta Q^{1/2} \left(\frac{T_2^*}{T_1}\right)^{1/2} (1 - E_2^2)^{1/2} G\,(x) \tag{15.3}$$

where

$$G\,(x) = \left[2\frac{1 - e^{-x}}{x\,(1+e^{-x})}\right]^{1/2} x = \frac{\mathrm{TR}}{\mathrm{T_1}} \text{ and } E_2^2 = exp\,(-2 \cdot a_t/T_2^*)\,, \tag{15.4}$$

C is the concentration of the nuclear spin under observation; a_t is the spectrum acquisition time; Q is the radio frequency (RF) coil quality factor. C and γ are B_0-independent and can be treated as constants.

Equation (15.3) accounts for most B_0-dependent parameters that have influences in the apparent SNR, such as T_2* signal loss and the partial saturation effect on signal due to a relatively short TR of $\ll 5T_1$. For in vivo ^{31}P MRS applications, the term of $(1 - E_2^2)^{1/2} G\,(TR/T_1)$ approximates to 1.0 (60), thus Eq. (15.5) is a simplification

$$SNR\,(\text{per unit sampling time}) \propto B_0^{\beta} Q^{1/2} \left(\frac{T_2^*}{T_1}\right)^{1/2}, \quad (15.5)$$

or

$$SNR\,(\text{per unit sampling time}) \propto B_0^{\beta*} \left(\frac{T_2^*}{T_1}\right)^{1/2}, \quad (15.6a)$$

if one applies the approximation of $Q \propto B_0^{1/2}$ resulting $\beta^* = \beta + 1/4$ (57,60). The values for β^* and β based on the theoretical predictions are 1.75 and 1.5 respectively (57).

For precisely quantifying and understanding the sensitivity of in vivo ^{31}P MRS as a function of magnetic field strength, it is necessary to quantify all B_0-dependent parameters used in Eq. (15.6A).

2.2.1. Field Dependence of in vivo ^{31}P MRS Sensitivity—It has been demonstrated that both SNR and the quality of in vivo ^{31}P MRS acquired in human brain are improved at higher fields (24,61–63). Recently, we have quantitatively measured and compared the values of T_1, T_2* and SNR of PCr resonance peak acquired from the human occipitallobe at 4 tesla and 7 tesla (60). We found that not only T_2* of PCr, but also T_1 of PCr (i.e. $T_{1,\mathrm{PCr}}$) were shortened at 7 tesla compared to 4 tesla. This observation indicates that the field dependence of $T_{1,\mathrm{PCr}}$ is likely determined by two competing relaxation mechanisms, *i.e.* the chemical shift anisotropy (CSA) and the dipolar interaction that simultaneously influence the ^{31}P longitudinal relaxation time (60,64,65). In the case with dominant CSA contribution, the T_1 value decreases with increasing field strength following the relation of $1/T_1 \propto \mathrm{B}_0^2$; in contrast, the T_1 value increases with increasing field strength when the dipolar interaction mechanism dominates. The opposite trends between these two relaxation mechanisms lead to a decrease in $T_{1,\mathrm{PCr}}$ at higher field and offer an advantage for in vivo ^{31}P MRS as a shorter repetition time can be employed which allows more signal averaging within the same sampling time; as a result, improving SNR and leading to a total SNR gain of 56% at 7T as compare to 4T. Moreover, the β value derived from the experimental measurements and Eq. (15.5) in this study was 1.4 (60). This value is in an excellent agreement with the theoretically predicted β value of 1.5 as described in the literature (57).

Another interesting observation of this study is that the linewidth broadening of the phosphate resonance peak with increased field strength is not linearly correlated with the field strength and, thus, at higher field strength, there is a small increase in the line width of phosphate signals (60). Moreover, higher field strength increases the chemical shift dispersion (i.e., in Hz unit) of in vivo ^{31}P MRS linearly with field strength. The combination of these two factors (i.e., large increase in chemical shift dispersion and relatively small increase in linewidth broadening) improves the ^{31}P spectral resolution at 7T (see Fig. 15.2A). This improvement makes it possible to resolve many adjacent phosphate metabolite resonance peaks (e.g., α-ATP versus NAD) and it is especially helpful for resolving the Pi

peak from other adjacent resonance peaks. The well-resolved Pi peak is crucial for measuring the ATP production flux and will be discussed later.

2.2.2. Field Dependence of in vivo ^{17}O MRS Sensitivity—^{17}O is a stable oxygen isotope with a spin quantum number of 5/2 and detectable by ^{17}O MRS. It possesses an electric quadrupolar moment and its natural abundance is only 0.037%, which is almost 30 times lower than that of ^{13}C and 2700 times lower than that of ^{1}H. Moreover, the γ value of ^{17}O is 7.4 times lower than that of ^{1}H. These factors attribute to the low inherent ^{17}O sensitivity that might be the major obstacle for the development and application of in vivo ^{17}O MRS approaches.

The relaxation mechanism of ^{17}O spin is distinct from ^{31}P spin. The ^{17}O quadrupolar moment can interact with local electric field gradients and the temporal fluctuations of this interaction induced by molecular motion dominate the ^{17}O relaxation processes and determine both T_1 and T_2 of H_2 ^{17}O (66), where T_2 is the transverse relaxation time. Theoretically, the T_1, T_2 and T_2* values of ^{17}O water spins are expected to be insensitive to B_0 (55, 66). We have experimentally investigated and compared the ^{17}O relaxation times of the natural abundance H_2 ^{17}O in rat brain at both 4.7 and 9.4 tesla. We confirmed that the ^{17}O relaxation times are B_0-independent (67). Recent experimental evidence has indicated that the B_0-independence of ^{17}O relaxivity can further extend to a much higher magnetic field, such as 17.6 tesla (68). The field independence of ^{17}O relaxivity reveals that ^{17}O sensitivity gain at higher fields is not compromised by the relaxation times, and this could lead to a substantial sensitivity gain when the field strength increases according to Eq. (15.6B) if the same acquisition parameters (e.g., TR and a_t) are applied at different field strengths,

$$SNR\,(\text{per unit sampling time}) \propto B_0^{\beta *}. \quad (15.6b)$$

Our experimental results showed approximately a four-fold SNR gain in the in vivo ^{17}O MRS signal measured in the rat brain at 9.4 tesla compared to 4.7 tesla (67). Moreover, the β* value deduced from these experimental measurements and Eq. (15.6B) was ~2 (67), which is close to the theoretically predicted β* value of 7/4 (57). The significant sensitivity gain provides adequate SNR for acquiring the 3 dimensional ^{17}O MRS imaging of the natural abundance $H_2{}^{17}$O from the small brain of rat with a temporal resolution of ~10 seconds at 9.4T (see one example shown in Fig. 15.2B).

Clearly, the increase of B_0 should benefit all of the in vivo multinuclear MRS approaches. In vivo ^{17}O MRS probably benefits the most from the substantial sensitivity gain at ultrahigh fields. On the other hand, in vivo ^{31}P MRS can benefit from both the moderate sensitivity gain and the significant spectral resolution improvement, which is crucial for resolving many overlapping resonance peaks of different metabolites. All these benefits provided by high field strength are essential for improving the reliability of in vivo ^{17}O and ^{31}P MRS and for accurately determining cerebral metabolic fluxes.

3. How to Apply In Vivo ^{17}O MRS for Imaging $CMRO_2$

In vivo ^{17}O MRS methodology has two major applications for studying brain function and cerebral bioenergetics through imaging either cerebral blood flow (CBF) or $CMRO_2$ (51–55, 67, 69–87). Both applications rely upon the measurement of brain $H_2{}^{17}O$ content and its dynamic change using in vivo ^{17}O MRS. The CBF measurement is based on monitoring the washout rates of inert $H_2{}^{17}O$ tracer in the brain tissue following an intravascular bolus injection of ^{17}O-labeled water. The $CMRO_2$ measurement is based on monitoring the dynamic changes of metabolically generated $H_2{}^{17}O$ in the brain tissue from inhaled ^{17}O-labeled oxygen gas (55). There are two types of magnetic resonance approaches for monitoring brain $H_2{}^{17}O$ in vivo: a direct approach by using ^{17}O MRS detection, and an indirect approach by using ^1H magnetic resonance imaging (MRI) to measure the changes in T_2- or $T_{1\rho}$-weighted proton signals caused by the ^{17}O-^1H scalar coupling and proton chemical exchange (see recent review article of (55) and the references cited therein). Both direct and indirect approaches are suitable for CBF measurements. However, recent studies indicated that the in vivo ^{17}O MRS approach at ultrahigh fields seems to have more advantages for quantifying and imaging $CMRO_2$, which perhaps is the most important application of in vivo ^{17}O MRS. Here, the in vivo ^{17}O MRS approach for imaging $CMRO_2$ is described in detail.

3.1. Theory and Quantification of $CMRO_2$ Based on In Vivo ^{17}O MRS Approach

In general, there is a similarity between in vivo ^{17}O MRS approach and positron emission tomography (PET) approach (88–91) for measuring $CMRO_2$ through the use of isotropic labeled oxygen gas ($^{17}O_2$ for MRS and $^{15}O_2$ for PET). After gas exchange in the lung, the inhaled and labeled O_2 molecules quickly bind to hemoglobin (Hb) in the blood, forming O_2-hemoglobin complexes (HbO_2) (see Fig. 15.1). Through the feeding arteries and arterioles, the HbO_2 complex enters the brain capillaries. The O_2 molecules are dissociated from hemoglobin in the capillaries, then cross the brain blood barrier (BBB) in the form of free gas, diffuse into the brain tissue (intra- and extracellular space), and finally enter mitochondria where they are metabolized and produce the water with the isotope label following the chemical reaction (3):

$$\text{Carbon substrate} + O_2 \rightarrow \text{Oxidized carbon substrate} + 2H_2O \quad (15.7)$$

According to this reaction (equivalent to **R1** in Fig. 15.1), one oxygen molecule produces two isotopic labeled water molecules ($H_2{}^{17}O$ for ^{17}O MRS and $H_2{}^{15}O$ for PET), which can move out of the mitochondria (traversing the opposite pathway as O_2 entry) and finally be washed out from the brain through venules and veins. The dynamic change of the isotope labeled water in the brain is tightly linked to the cerebral oxygen utilization rate. It provides the vital signal source for determining $CMRO_2$ for both ^{15}O PET and ^{17}O MRS.

Though the principle underlying the ^{17}O MRS approach for measuring $CMRO_2$ was historically adopted from the well-established ^{15}O PET approach, there is significant distinction between these two neuroimaging approaches. For instance, one complication in PET is that it is unable to distinguish the ^{15}O signal contribution from $^{15}O_2$ molecules

versus the metabolically generated $H_2{}^{15}O$ molecules. This limits the robustness of PET technique for imaging $CMRO_2$ (55, 90). In contrast, the ^{17}O MRS approach specifically detects the metabolically generated $H_2{}^{17}O$ without confounding signals from $^{17}O_2$ molecules because of the "invisibility" of $^{17}O_2$ in an in vivo ^{17}O spectrum (55). This unique magnetic resonance specificity leads to a great advantage which significantly simplifies the in vivo ^{17}O MRS methodology for measuring and quantifying $CMRO_2$ (55, 87). Nevertheless, the dynamic change of the metabolically generated $H_2{}^{17}O$ concentration in the brain during an $^{17}O_2$ inhalation is interplayed by three parallel processes (see Fig. 15.3): (i) Cerebral oxygen utilization for generating the metabolic $H_2{}^{17}O$ in the brain tissue, (ii) Cerebral blood perfusion resulting in $H_2{}^{17}O$ washout from the brain, and (iii) Blood recirculation bringing the metabolically generated $H_2{}^{17}O$ in the entire body back to the brain. All contributions from these three processes have to be considered for quantifying $CMRO_2$. Based on the Kety – Schmidt theory (92–94), the mass balance of the isotope labeled $H_2{}^{17}O$ in the brain tissue during an $^{17}O_2$ gas inhalation can be derived as (52,54,55,87):

$$\frac{dCb\,(t)}{dt}=2\alpha f_1\,CMRO_2+mCBF\left(f_2Ca\,(t)-\frac{nCb\,(t)}{\lambda}\right) \quad (15.8)$$

where $C_a(t)$, $C_b(t)$ and $C_v(t)$ are the metabolic $H_2{}^{17}O$ concentrations in excess of the natural abundance of $H_2{}^{17}O$ concentration in the arterial blood, brain tissue and venous blood respectively, as a function of $^{17}O_2$ inhalation time (t, unit = minute); α is the ^{17}O enrichment fraction of the oxygen atoms in the inhaled $^{17}O_2$ gas; λ is the brain/blood partition coefficient (95). The factor of two accounts for the fact that one O_2 converts to two H_2O molecules through oxidative metabolism according to Eq. (15.7); f_1 and f_2 are two unit conversion factors (54, 87). The correction factor m is used in Eq. (15.8) to account for the water permeability restriction across the brain blood barrier (96), and n is another correction factor that accounts for the permeability restriction occurring when $H_2{}^{17}O$ molecules which are metabolically generated inside the mitochondria across the mitochondrial membranes (54,87). Both m and n depend on CBF (54,87). The function of $C_a(t)$ (or artery input function) is determined by the total metabolic $H_2{}^{17}O$ generated in all aerobic organs of a living body. It can approximate as a linear function of $^{17}O_2$ inhalation time (i.e., $C_a(t)=At$, A is a constant) (52, 54, 78, 87). Under this approximation, the solution for solving the differential equation of Eq. (15.8) is:

$$CMRO_2\,(t)=\frac{\left\{\left[\frac{C_b(t)-\frac{Af_2\lambda^2}{mn^2CBF}\left(\frac{mnCBF}{\lambda}te^{-\frac{mnCBF}{\lambda}t}+e^{-\frac{mnCBF}{\lambda}t}-1\right)}{1-e^{-\frac{mnCBF}{\lambda}t}}\right]-\frac{Af_2\lambda t}{n}\right\}}{\frac{2\alpha\lambda f_1}{mnCBF}}. \quad (15.9)$$

According to this equation, the $CMRO_2$ value at *each* data point measured at different inhalation time (t) can be calculated by using the experimentally measured CBF, A, n, $C_b(t)$ values and other known constants (f_1, f_2, m, α and λ). The quantification approach based on

Eq. (15.9) is a complete model which accounts for all required parameters for precisely determining $CMRO_2$ (54,55,87).

3.2. Measurement and Imaging of $CMRO_2$ using In Vivo $^{17}O_{MRS}$ Approach

The complete model as described by Eq. (15.9) requires multiple experimental measurements of four variables (A, n and $C_b(t)$ and CBF) in order to calculate $CMRO_2$. Figure 15.4 illustrates the procedures for performing these in vivo ^{17}O MRS measurements and the results of a rat brain study with α-chloralose anesthesia at 9.4 T (54,55).

3.2.1. Imaging CBF—The CBF measurement was performed via bolus injection of a small amount of ^{17}O-enriched water into one internal carotid artery and monitoring the washout process of the $H_2\,^{17}O$ tracer in the brain using 3 dimensional ^{17}O chemical shift imaging (CSI) (67). Figure 15.4A demonstrates the stacked plots of $H_2\,^{17}O$ spectra acquired from a single voxel (as indicated in the brain anatomy image) of 3 dimensional ^{17}O CSI data set in a representative rat before and after the $H_2\,^{17}O$ bolus injection. The peak height of the $H_2\,^{17}O$ spectra shows an exponential decay and its decay rate determines the CBF value in the CSI voxel (54,55,67).

3.2.2. Imaging $C_b(t)$—The crucial step for $CMRO_2$ measurements is to monitor and image the dynamic changes of the metabolic $H_2\,^{17}O$ content in the brain (i.e., $C_b(t)$) during an inhalation of $^{17}O_2$ gas. Figure 15.4B illustrates the stacked plots of ^{17}O spectra of cerebral $H_2\,^{17}O$ from the CSI voxel acquired before, during and after a 2-minute inhalation of $^{17}O_2$ (54). It indicates excellent ^{17}O sensitivity for detecting the cerebral $H_2\,^{17}O$ signal and its change during the inhalation; and the approximately linear increase of $H_2\,^{17}O$ during a short $^{17}O_2$ inhalation is evident, and the slope is tightly coupled to $CMRO_2$.

One practical challenge for most in vivo MRS approaches is the difficulty for measuring the absolute concentrations of metabolites of interest. Nevertheless, the natural abundance $H_2\,^{17}O$ signal which can be accurately measured in the brain before the introduction of ^{17}O-labeled oxygen gas (see Fig. 15.4B) provides an excellent internal reference for quantifying the absolute concentration of $C_b(t)$ for each CSI voxel (54, 87). This self-calibration method is independent of the ^{17}O detection sensitivity. This is particularly valuable when a surface RF coil with nonuniform spatial distribution of detection sensitivity is applied.

3.2.3. Other Measurements—The arterial input function of $C_a(t)$ was measured in vivo by an implanted ^{17}O RF coil (97) wrapped around a carotid artery (in the rat). Figure 15.4C illustrates the implanted ^{17}O RF coil, the natural abundance $H_2\,^{17}O$ signal detected from the rat carotid blood and $C_a(t)$ measured during a two-minute inhalation of $^{17}O_2$ (54). The experimental result showed an approximately linear relation between the arterial $H_2\,^{17}O$ concentration and the $^{17}O_2$ inhalation time, and the linear fitting of $C_a(t)$ gave the value of constant A required by Eq. (15.9). Note that the $C_a(t)$ (see Fig. 15.4C) and $C_b(t)$ (see Fig. 15.4B) measurements could be conducted simultaneously with the configuration of dual ^{17}O RF coils and receivers (97).

Finally, the ratio between the decay rates of $H_2\,^{17}O$ signal measured after the cessation of $^{17}O_2$ inhalation (see Fig. 15.4B) versus that after a $H_2\,^{17}O$ bolus injection (see Fig.

15.4A) gives the constant of n, reflecting the H_2 ^{17}O permeability restriction across the mitochondrial membranes (54,87).

3.2.4. Imaging $CMRO_2$ in Rat Brain—The values of $C_b(t)$, CBF and n measured from each ^{17}O MRS imaging (MRSI) voxel and the value of A measured from each ^{17}O inhalation measurement in the same animal as demonstrated in Fig. 15.4 can be used to calculate the absolute $CMRO_2$ value as a function of inhalation time according to Eq. 15.9. Figure 15.5A shows one example of $CMRO_2$ time course from a representative ^{17}O MRSI voxel with a temporal resolution of 11 seconds (54). It is evident that the $CMRO_2$ values are independent of $^{17}O_2$ inhalation time if the first two $CMRO_2$ values characterized with relatively large fluctuations are excluded. These $CMRO_2$ values were averaged for improving measurement accuracy. The same procedure and calculation can be applied to all ^{17}O MRSI voxels for generating 3D $CMRO_2$ images in the rat brain (54, 77). Figure 15.5B demonstrates three adjacent $CMRO_2$ images in the coronal orientation from a representative rat brain. The averaged $CMRO_2$ and CBF values in the rat brains anesthetized with α-chloralose were 2.19 ± 0.14 μmol/g/min and 0.53 ± 0.07 ml/g/min (n=7), respectively (54). The $CMRO_2$ value is consistent with the reported values in the literature, which were measured by other independent techniques under similar physiological condition (98–100).

3.3. Establishing a Robust and Noninvasive ^{17}O MRS Approach for Imaging $CMRO_2$

3.3.1. Noninvasive Approach—The major technical limitation of the complete model for determining $CMRO_2$ using in vivo ^{17}O MRS is the requirement of invasive measurements (e.g., CBF, $C_a(t)$, n). This could significantly limit the potential of this in vivo approach for broad biomedical applications, especially in humans. Thus, it is crucial to examine the feasibility of developing a completely noninvasive ^{17}O approach for imaging $CMRO_2$. Attempts have been made to simplify the experimental procedures and the models for determining $CMRO_2$ based on a number of approximations (52, 53, 73, 79, 81, 87). We discuss one of these models, in which the invasive measurements could be eliminated by using the simplified model based on the Taylor's and Polynomial Theorems (87). Briefly, the $C_b(t)$ time course can be expressed by a polynomial expansion

$$C_b(t) = a_1 t + a_2 t^2 + a_3 t^3 + \cdots \quad (15.10)$$

In this expansion, the first-order (or linear) coefficient of a_1 is directly proportional to $CMRO_2$ according to the following equation (87)

$$CMRO_2 = \frac{a_1}{2\alpha f_1} \quad (15.11)$$

where α and f_1 are known constants (see above). Thus, using this *simplified model*, only the time course of $C_b(t)$ measured noninvasively by in vivo ^{17}O CSI approach is needed and it can be fitted to the polynomial function given by Eq. (15.10) to calculate the linear coefficient of a_1, and ultimately determining $CMRO_2$ according to Eq. (15.11). For practical

applications, a quadratic polynomial function provides a good approximation for fitting the time course of $C_b(t)$ with moderate measurement fluctuation (101). We have demonstrated that the $CMRO_2$ value obtained based on the complete model with invasive procedures has no statistical difference from that based on the simplified model and quadratic function fitting where only a single noninvasive measurement of $C_b(t)$ is required (87). Moreover, our results also validated that the linear fitting of $C_b(t)$ could provide a good approximation for determining $CMRO_2$ in the rat brain when the $^{17}O_2$ inhalation time is relatively short (e.g., 2 minutes) (87). This is consistent with the prediction based on either Eq. (15.8) or (15.10). During the initial $^{17}O_2$ inhalation period, both $C_a(t)$ and $C_b(t)$ have not built up significantly resulting in near zero value of the second term on the right side of Eq. (15.8). Therefore, Eq. (15.8) can be approximated as a linear differential equation, and $C_b(t)$ becomes a linear function of the inhalation time. This is also evident in Eq. (15.10) in which the high-order terms become negligible when t is short. Therefore, it is possible to use the simplified model for determining and imaging $CMRO_2$ based on a single and completely noninvasive ^{17}O spectroscopic imaging measurement of $C_b(t)$ (55,86,87).

Recently, we have further examined the simplified model for determining $CMRO_2$ under varied physiological conditions (86). In this study, we compared the $CMRO_2$ results obtained with the complete model versus the simplified model using linear fitting of $C_b(t)$ under normothermia (37°C) condition and hypothermia (32°C) condition, which is a well known factor leading to significant suppression of both CBF and $CMRO_2$. Figure 15.6 demonstrates an excellent consistency of the $CMRO_2$ results between the complete and simplified models for either the voxel-wised comparison (Fig. 15.6A) or the averaged $CMRO_2$ comparison (Fig. 15.6B) at both brain temperatures (86). The comparison results reveal the validity of the simplified ^{17}O approach for imaging $CMRO_2$ applicable at a wide physiological range. Additional technical development which further advances the in vivo ^{17}O methodology could ultimately provide the simplest and completely noninvasively ^{17}O neuroimaging approach for imaging $CMRO_2$ (in humans).

3.3.2. Robustness and Reliability—Another merit of the ^{17}O $CMRO_2$ imaging approach is its ability for performing repeated $CMRO_2$ imaging measurements with a short interval between two measurements. This is due to the fact that the cerebral $H_2{}^{17}O$ concentration can quickly reach a new and steady level within a few minutes after the cessation of $^{17}O_2$ inhalation, which allows repeated $CMRO_2$ measurements in the same subject and experimental session (see Fig. 15.7A). Figure 15.7B shows the excellent reproducibility of repeated $CMRO_2$ measurements in five rats (1st and 2nd measured $CMRO_2$ values were 2.26 ± 0.18 and 2.20 ± 0.14 μmol/g/min giving a ratio of 1.03 ± 0.05 between the consecutive measurements) (86). The results demonstrate the robustness and reliability of the simplified in vivo ^{17}O approach for noninvasively and rapidly imaging $CMRO_2$ repeatedly in a small brain of rat. This capability is particularly valuable for studies aiming at $CMRO_2$ changes induced by physiological or pathological perturbations in which multiple measurements are required under different conditions (e.g., control versus stimulation for brain function study). Therefore, the combination of the simplified model and ultrahigh field in vivo ^{17}O MRS may potentially provide an alternative neuroimaging

modality for studying the central role of oxidative metabolism in brain function and neurological diseases (55,77).

3.3.3. Demonstration of in vivo ^{17}O MRS Application for Studying Brain Bioenergetics—It is well documented that the basal $CMRO_2$ is sensitive to the brain temperature (see (3, 102) and the references cited therein). However, most studies reported in the literature were based on the global $CMRO_2$ measurements of entire brain using the Kety-Schmidt method (92, 93), and were limited by the lack of spatial information regarding regional $CMRO_2$. We have conducted a $CMRO_2$ imaging study using 3D in vivo ^{17}O CSI combined with the simplified model at 9.4 tesla for quantifying absolute $CMRO_2$ values in the rat brain at normal brain temperature (37°C) (i.e., normothermia) and mild hypothermia (32°C) conditions (86). Figure 15.8A illustrates an example showing three representative slices of 3D $CMRO_2$ maps from a rat brain under normothermic and hypothermic conditions. These images clearly show significant reduction of $CMRO_2$ crossing the entire brain induced by lowering brain temperature several degrees. This metabolic suppression occurring at hypothermia was consistently observed in all five rats studied (Fig. 15.8B), resulting in an average of 45% $CMRO_2$ reduction as compared to normothermic condition (86). These results indicate that the established in vivo ^{17}O MRS approach is sensitive to determine the dynamic $CMRO_2$ change and its spatial distribution due to physiological perturbation. The measured $CMRO_2$ can be quantitatively correlated to other associated physiological parameter changes. Figure 15.9 illustrates one example showing the quantitative relation between $CMRO_2$ and CBF: both of them were measured by in vivo ^{17}O MRS in the α-chloralose anesthetized rat under a wide range of physiological conditions from normothermia to hypothermia (86). It shows a strong correlation between CBF and $CMRO_2$ with a linear correlation coefficient of R = 0.97 indicating a tight vascular-metabolic coupling in the rat brain.

4. How to Apply In Vivo ^{31}P MRS for Studying Cerebral ATP Metabolic Fluxes and Bioenergetics

The ATP metabolism for regulating both ATP production and utilization plays a fundamental role in cerebral bioenergetics, brain function and neurodegenerative diseases. Two important chemical reactions that contribute to the brain ATP metabolism are the ATP_{ase} and CK reactions. They are coupled together and constitute a three-^{31}P-spin chemical exchange system involving ATP, PCr and Pi (i.e., PCr↔ATP↔Pi). One vital function of this exchange system is to maintain a stable cellular ATP concentration ensuring continuous energy supply for sustaining electro-physiological activity in the brain. Logically, the measures of ATP metabolic fluxes should be more sensitive to the brain activity and energy state and their change than that of steady-state ATP and other HEP concentration. Therefore, they should provide a useful index reflecting cerebral bioenergetics under various brain states. It would be, thus, essential to find a noninvasive and reliable technique being able to assess the cellular exchange rates (or fluxes) of PCr↔ATP↔Pi in brain *in situ*. The sole approach for serving this purpose is the use of in vivo ^{31}P MRS combined with magnetization transfer method (20,43–47,50,103). However, to completely determine the kinetics and fluxes involved in the PCr↔ATP↔Pi exchange requires extensive measurements and information

including three steady-state phosphate metabolite concentrations (i.e., [ATP], [PCr] and [Pi]) and their intrinsic T_1 values, and four pseudo first-order chemical reaction rate constants (forward and reverse rate constants for the CK reaction and the ATP_{ase} reaction, respectively) (50). The products of the rate constants and their related phosphate concentrations can provide four ATP metabolic fluxes along both forward and reverse reaction directions in the $PCr \leftrightarrow ATP \leftrightarrow Pi$ exchange system (see Fig. 15.10).

Several in vivo ^{31}P MT methods have been developed such as conventional two-spin magnetization saturation transfer (CST), inversion recovery transfer (IT) and two-dimensional chemical exchange spectroscopy (2D-EXSY) (44, 45, 49, 104). They have been applied to physiological studies of ATP metabolism in a variety of organs, from hearts to brains (20, 24, 45, 46, 49, 50, 103, 105–111). Among these methods, the CST method is most commonly used in biomedical research, perhaps due to its methodological simplicity and high efficiency. This method is particularly useful in measuring the forward rate constants and fluxes in the chemical exchange system of $PCr \leftrightarrow ATP \leftrightarrow Pi$ when a frequency-selective RF saturation pulse train is applied to fully saturate the γ-ATP spin. Under this circumstance, the three-spin chemical exchange system of $PCr \leftrightarrow ATP \leftrightarrow Pi$ can be treated as two independent two-spin chemical exchange systems (i.e., $PCr \leftrightarrow ATP$ and $ATP \leftrightarrow Pi$); consequently, the forward rate constants and fluxes for both the CK reaction (i.e., **R4** in Figs. 15.1 and 15.13) and ATP_{ase} reaction (i.e., **R2** in Figs. 15.1 and 15.13) can be explicitly determined. These forward metabolic fluxes reflect the ATP synthesis or production rates catalyzed by ATP_{ase} and CK, respectively. However, the measurements of the reverse CK flux ($ATP \rightarrow PCr$) using CST (i.e., by saturating PCr) resulted in an inequality between the forward and reverse CK fluxes (112–114), which is paradoxical, in the sense that the CK fluxes into and out of the PCr pool must be equal when the CK reaction is under chemical equilibrium condition. One possible explanation is that the ATP metabolism involves other chemical exchange reactions besides the CK reaction, for example the ATP hydrolysis reaction (115). Consequently, neglecting ATP hydrolysis may lead to an error in estimating the reverse CK flux. Therefore, it is necessary to consider $PCr \rightarrow ATP \leftrightarrow Pi$ as a three-spin chemical exchange system in order to accurately determine all kinetic parameters; in particular, the reverse rate constants and fluxes (45,46,50,115,116).

We will discuss a newly introduced in vivo ^{31}P MT approach being able to noninvasively study the $PCr \leftrightarrow ATP \leftrightarrow Pi$ exchange in the brain explicitly through the in vivo measurements of the following rate constants and fluxes associated with four coupled reactions in different subcellular compartments (50):

- **i.** The forward flux $(F_f^{ATP_{ase}})$ of ATP_{ase} reaction (i.e., **R2** in Figs. 15.1 and 15.13) occurring inside the mitochondria;
- **ii.** The forward flux (F_f^{CK}) of CK reaction (i.e., **R4** in Figs. 15.1 and 15.13),
- **iii.** The reverse flux $(F_r^{ATP_{ase}})$ of ATP_{ase} reaction (i.e., **R5** in Figs. 15.1 and 15.13) occurring in the cytosol space;
- **iv.** The reverse flux (F_r^{CK}) of CK reaction (i.e., **R3** in Figs. 15.1 and 15.13).

4.1. In vivo ^{31}P MT Approach for Determining Entire PCr↔ATP↔Pi Exchange

A newly introduced in vivo ^{31}P MT approach for determining all kinetic parameters of the *PCr↔ATP↔Pi* exchange is called the Multiple Single-site Saturation (MSS) MT approach (50). The MSS approach requires a total of four in vivo ^{31}P spectra: one control spectrum in the absence of RF saturation plus three single-site, RF-saturated spectra with the saturation frequency on PCr, γ-ATP and Pi, respectively (50). The quantification of the ATP metabolic fluxes relies on solving three coupled Bloch equations based on the three-spin chemical exchange model. For simplifying the mathematical derivation, the symbols of a, b and c were used which stand for PCr, ATP and Pi, respectively. The Bloch equations describing the magnetizations of a, b and c and their changes as a function of time are given by (43),

$$\begin{array}{ccccc} \mathrm{PCr} & \underset{k_1}{\overset{k_{-1}}{\rightleftarrows}} & \gamma-ATP & \underset{k_2}{\overset{k_{-2}}{\rightleftarrows}} & P_i \\ a & & b & & c \end{array}$$

$$\frac{dM_a}{dt} = -\frac{(M_a - M_a^0)}{T_{1a}} - k_1 M_a + k_{-1} M_b \quad (15.12a)$$

$$\frac{dM_b}{dt} = -\frac{(M_b - M_b^0)}{T_{1b}} - k_{-1} M_b - k_2 M_b + k_1 M_a + k_{-2} M_c \quad (15.12b)$$

$$\frac{dM_c}{dt} = -\frac{(M_c - M_c^0)}{T_{1c}} - k_{-2} M_c + k_2 M_b \quad (15.12c)$$

where M_a, M_b and M_c are the magnetizations of PCr, γ-ATP and Pi; M_a^0, M_b^0 and M_c^0 are the magnetizations at Boltzmann thermal equilibrium; k_1 and k_{-2} are the pseudo first-order forward rate constants involving ATP production through the CK reaction and the ATP_{ase} reaction, respectively; k_{-1} and k_2 are the pseudo first-order reverse rate constants involving ATP utilization through the CK reaction and the ATP_{ase} reaction, respectively; T_{1a}, T_{1b} and T_{1c} are the intrinsic spin-lattice relaxation times of PCr, γ-ATP and Pi, which are B_0 dependent. Four rate constants involving the *PCr↔ATP↔Pi* exchange and their four associated ATP metabolic fluxes can be determined by the following three-step measurements with frequency-selective RF saturation on the γ-ATP (Step 1), Pi (Step 2) and PCr (Step 3) resonance peak, respectively.

Step 1: Progressive saturation of γ-ATP for determining intrinsic spin-lattice relaxation times of PCr and Pi, forward rate constants and fluxes—The first step of the ^{31}P MT measurements is to apply a frequency-selective RF pulse train for completely saturating the γ-ATP resonance peak with varied saturation time (*t*) (i.e., the progressive saturation experiment commonly used in the CST approach). For this case, the three-spin chemical exchange system of *PCr↔ATP↔Pi* can be treated as two independent two-spin chemical exchange systems (i.e., *PCr↔ATP* and *ATP↔Pi*) Solving Eqs. (15.12a) and (15.12c) with the boundary condition of *Mb* = 0 results in Eqs. (15.13a) and (15.13b) (47),

$$M_a(t) = M_a^0 \left[\left(\frac{k_1}{\alpha_a} \right) e^{-\alpha_a t} + \left(\frac{1}{\alpha_a T_{1a}} \right) \right] \quad (15.13a)$$

$$M_c(t) = M_c^0 \left[\left(\frac{k_{-2}}{\alpha_c} \right) e^{-\alpha_c t} + \left(\frac{1}{\alpha_c T_{1c}} \right) \right] \quad (15.13b)$$

with

$$\alpha_a = \frac{1}{T_{1a}^{app}} = \left(k_1 + \frac{1}{T_{1a}} \right); \alpha_c = \frac{1}{T_{1c}^{app}} = \left(k_{-2} + \frac{1}{T_{1c}} \right).$$

Therefore, the parameters of apparent spin-lattice relaxation rates (α_a and α_c) and intrinsic spin-lattice relaxation times (T_{1a} and T_{1c}) at a given B_0 can be determined via regressions as a function of t, where both k_1 and k_{-2} are replaced by their apparent spin-lattice relaxation rate and intrinsic spin-lattice relaxation time (see Eqs. (15.13a) and (15.13b)). Then, the forward rate constants (k_1 and $k_{-}2$) can be calculated by their relations with the apparent spin-lattice relaxation rate and intrinsic spin-lattice relaxation time as depicted above.

When a steady-state condition is approached with complete saturation of γ-ATP (i.e., $dM_a/dt = 0$ and $dM_c/dt = 0$), Eqs. (15.13a) and (15.13b) can be further simplified to the following formulae:

$$k_1 = \frac{M_a^0 - M_a^{*b}}{M_a^0} \alpha_a = \frac{M_a^0 - M_a^{*b}}{T_{1a} M_a^{*b}} \quad (15.13c)$$

$$k_{-2} = \frac{M_c^0 - M_c^{*b}}{M_c^0} \alpha_c = \frac{M_c^0 - M_c^{*b}}{T_{1c} M_c^{*b}} \quad (15.13d)$$

where M_a^{*b} and M_c^{*b} are the steady-state magnetizations of a and c when b is fully saturated. Therefore, the forward rate constants of k_1 and k_{-2} can be calculated by using Eqs. (15.13c) and (15.13d). For this case, only two steady-state spectra acquired in the presence and absence of saturating b are needed to determine both k_1 and k_{-2}, if T_{1a} and T_{1c} have already been determined at a given B_0 through the progressive saturation measurement accordingly to Eqs. (15.13a) and (15.13b). Finally, the forward fluxes for the CK and ATP_{ase} reactions can be determined by the following relations,

$$F_f^{CK} = k_1 [PCr] \text{ and } F_f^{ATP_{ase}} = k_{-2} [Pi] \quad (15.13e)$$

Step 2: Steady-state saturation of Pi for determining CK reverse rate constant and flux—The second step of the in vivo ^{31}P MSS MT measurements is to apply a frequency-selective RF pulse train for completely saturating the Pi resonance peak with a sufficiently long saturation time resulting in steady-state magnetizations of a and b. For this case, $M_c = 0$, $dM_a/dt = 0$, $dM_b/dt = 0$, and Eqs. (15.12a) and (15.12b) yield

$$k_{-1}=\alpha_a\left(\frac{M_a^{*c}}{M_a^0}-\frac{1}{T_{1a}\alpha_a}\right)\frac{M_a^0}{M_b^{*c}} \quad (15.14a)$$

$$k_1=\alpha_b\left(\frac{M_b^{*c}}{M_b^0}-\frac{1}{T_{1b}\alpha_b}\right)\frac{M_b^0}{M_a^{*c}} \quad (15.14b)$$

with

$$\alpha_b=\frac{1}{T_{1b}^{app}}=\left(k_2+k_{-1}+\frac{1}{T_{1b}}\right)$$

where M_a^{*c} and M_b^{*c} are the steady-state magnetizations of a and b when Pi is fully saturated. Only Eq. (15.14a) is needed in the MSS MT approach to determine the CK reverse rate constant (k_{-1}) by using the measured magnetizations (i.e., M_a^0, M_a^{*c} and M_b^{*c}) and other relaxation parameters (i.e., α_a and T_{1a}), which are determined by the measurement in Step 1. The reverse flux of CK reaction can be calculated by the following relation:

$$F_r^{CK}=k_{-1}\,[ATP]\,. \quad (15.14c)$$

Step 3: Steady-state saturation of PCr for determining ATP$_{ase}$ reverse rate constant and flux—The third step of the in vivo ^{31}P MSS MT measurements is to apply a frequency-selective RF pulse train for completely saturating the PCr resonance peak with a sufficiently long saturation time resulting in steady-state magnetizations of b and c. For this case, M_a=0, dM_b/dt=

$$k_2=\alpha_c\left(\frac{M_c^{*a}}{M_c^0}-\frac{1}{T_{1c}\alpha_c}\right)\frac{M_c^0}{M_b^{*a}} \quad (15.15a)$$

$$k_{-2}=\alpha_b\left(\frac{M_b^{*a}}{M_b^0}-\frac{1}{T_{1b}\alpha_b}\right)\frac{M_b^0}{M_c^{*a}} \quad (15.15b)$$

where M_b^{*a} and M_c^{*a} are the steady-state magnetizations of b and c when PCr is fully saturated. Only Eq. (15.15a) is needed in the MSS MT approach to determine the ATP_{ase} forward rate constant (k_2) by using the measured magnetizations (i.e., M_a^0, M_a^{*c} and M_b^{*c}) and other relaxation parameters (i.e., α_c and T_{1c}), which are determined by the measurement in Step 1. The reverse flux of the ATP_{ase} reaction can be calculated via following relation:

$$F_r^{ATP_{ase}} = k_2 [ATP]. \quad (15.15c)$$

Therefore, by combining these three measurement steps, one is able to measure all kinetic parameters which determine the entire exchange of $PCr \leftrightarrow ATP \leftrightarrow Pi$ including all four ATP metabolic fluxes for both forward and reverse reaction directions as schematically summarized in Figs. 15.1 and 15.13. In total, a minimal number of three selective saturated in vivo ^{31}P spectra plus one control in vivo ^{31}P spectrum (for quantifying [ATP], [Pi], [PCr], i.e., M_a^0, M_b^0 and M_c^0) are required by the MSS MT approach for the measurements (50).

4.2. Application of in vivo ^{31}P MSS MT Approach in Human Brain at 7T

The in vivo ^{31}P MT measurements can significantly benefit from the high-field advantages of improved MR detection sensitivity and spectral resolution. We have conducted extensive measurements at 7T for validating the in vivo ^{31}P MSS MT approach, and ultimately, determining the entire chemical exchange of $PCr \leftrightarrow ATP \leftrightarrow Pi$ in the human occipital lobe (20,50).

4.2.1. Progressive Saturation for Measuring Intrinsic T_1, Forward Rate Constants And Fluxes—Figure 15.10A illustrates the progressive saturation transfer measurements and related in vivo ^{31}P spectra when the γ-ATP resonance peak was completely saturated (i.e., Step 1 measurement used in the in vivo ^{31}P MSS MT approach). It shows a gradual decrease of Pi signal when the γ-ATP saturation time increases because of the chemical exchange between γ-ATP and Pi (i.e., $ATP \leftrightarrow Pi$) and the increased magnetization transfer effect (20). This MT effect was observed on the chemical-exchangeable Pi resonance but not for those adjacent and non-chemical-exchangeable phosphate metabolites such as PDE and PME groups. Moreover, the MT effect on Pi disappeared when the RF saturation frequency was moved to the opposite side of the in vivo ^{31}P spectrum with the same chemical shift difference as shown in Figure 15.10B. Figure 15.10C plots the quantitative relation between the normalized Pi signal intensity (i.e., $M_a^{(t)}/M_a^0$ in Eq. (15.13a)) under the γ-ATP saturation with the saturation time of t. This plot can be used to calculate the intrinsic T_1 of Pi (i.e., T_{1a}) and the forward ATP_{ase} reaction rate constant (k_1) by the regression fitting according to Eq. (15.13a). Then, the forward ATP_{ase} reaction flux can be determined according to Eq. (15.13e). The same in vivo ^{31}P MT spectral data can be applied to quantify the MT effect on the PCr resonance as a function of the γ-ATP saturation time, ultimately, to determine the intrinsic T_1 of PCr (i.e., T_{1c}) and the forward CK reaction rate constant and flux according to Eqs. (15.13b) and (15.13e).

4.2.2. Steady-State Saturation for Measuring Forward Rate Constants And Fluxes—

One technical limitation of progressive saturation approach is the requirement of a number of saturated in vivo ^{31}P spectra with varied saturation time (e.g., Fig. 15.10). One alternative but more robust approach is the use of steady-state saturation if the intrinsic T_1 values have been determined at a given B_0 (see details in the discussion of Step 1 measurement above). Figure 15.11 demonstrates such a measurement (i.e., Step 1) and the in vivo ^{31}P MT spectra acquired in the absence (control spectrum; Fig. 15.11A) and presence (saturated spectrum; Fig. 15.11B) of sufficiently long RF saturation for ensuring complete saturation of the γ-ATP resonance peak and approaching steady-state magnetizations for both Pi and PCr. Figure 15.11C shows the difference spectrum by subtracting the control and γ-ATP saturated spectra (20, 50). The relative Pi signal reduction can be used to calculate the forward rate constant and flux for the ATP$_{ase}$ reaction according to Eqs. (15.13d) and (15.13e). Similarly, the relative PCr signal reduction can be used to calculate the forward rate constant and flux for the CK reaction according to Eqs. (15.13c) and (15.13e).

4.2.3. In vivo ^{31}P MSS MT Measurements for Determining all ATP Metabolic Fluxes Involving PCr↔ATP↔Pi Exchange in Human Occipital Lobe—

Figure 15.12 illustrates one example of in vivo ^{31}P MSS MT measurements in the human occipital lobe (50). A total of four in vivo ^{31}P spectra were collected in the absence (Fig. 15.12A) and presence of complete RF saturation on the resonance peak of Pi (Step 2; Fig. 15.12B), PCr (Step 3; Fig. 15.12C) and γ-ATP (Step 1; Fig. 15.12D), respectively. It reveals that single-site saturation on one phosphate spin can lead to significant magnetization reductions in the other two coupled phosphate spins through the three-spin chemical exchange system of *PCr↔ATP↔Pi*. For instance, the PCr saturation results in a significant signal reduction for both γ-ATP and Pi as shown in Fig. 15.12C. All required steady-state saturated magnetizations can be determined by using the three saturated in vivo ^{31}P spectra as shown in Fig. 15.12B–D, and all equilibrium magnetizations can be determined by using the control in vivo ^{31}P spectrum as shown Fig. 15.12A. The values of these magnetizations were used to determine four rate constants (k_1, k_2, k_{-1} and k_{-2}) and four fluxes ($F_f^{ATP_{ase}}$, $F_r^{ATP_{ase}}$, F_f^{CK} and F_r^{CK} associated with the *PCr↔ATP↔Pi* exchange in the human brain. These measured results and the ratios between the forward and reverse fluxes are summarized in Fig. 15.13 indicating several important observations. First, there is no statistical difference between the forward and reverse exchange fluxes for both the CK reaction (i.e., F_f^{CK} versus F_r^{CK}; $p = 0.38$) and the ATP$_{ase}$ reaction (i.e., $F_f^{ATP_{ase}}$ versus $F_r^{ATP_{ase}}$; $p = 0.46$) (50). Second, the ratios between the forward and reverse fluxes for the CK reaction $(F_f^{CK}/F_r^{CK} = 0.95 \pm 0.12)$ and the ATP$_{ase}$ reaction $(F_f^{ATP_{ase}}/F_r^{ATP_{ase}} = 1.08 \pm 0.21)$ are close to unity. In general, the CK fluxes reflect the nonoxidative phosphorylation and the ATP$_{ase}$ fluxes, in contrast, reflect oxidative phosphorylation. Both of these phosphorylation pathways can contribute to the total ATP production flux (i.e., $F_f^{total} = F_f^{CK} + F_f^{ATP_{ase}} = 73.9\ \mu\mathrm{mol}/g/min$) and the total ATP utilization flux (i.e., $F_r^{total} = F_r^{CK} + F_r^{ATP_{ase}} = 76.9\ \mu\mathrm{mol}/g/min$). The ratio between F_f^{total} and F_r^{total} is again close to unity (=0.96) indicating that the total ATP production flux equals

the total ATP utilization flux. These results lead us to conclude that the fluxes measured by the in vivo ^{31}P MSS MT approach satisfy the chemical equilibrium conditions for the CK and ATP_{ase} reactions in the human brain, and indicate that the MSS MT approach is able to explicitly determine four rate constants in the $PCr \leftrightarrow ATP \leftrightarrow Pi$ kinetic process and their associated ATP metabolic fluxes in the brain noninvasively. Nevertheless, such equal forward and reverse flux relations are unable to be obtained for the saturation transfer measurement if the three-spin $PCr \leftrightarrow ATP \leftrightarrow Pi$ exchange system was treated as two independent two-spin change systems (i.e., $PCr \leftrightarrow ATP$ and $ATP \leftrightarrow Pi$) even when the same experimental MSS MT data were analyzed (50). These findings clearly indicate that the chemical exchange system of $PCr \leftrightarrow ATP \leftrightarrow Pi$ has to be treated as a three-spin exchange system in order to accurately determine the reverse rate constants and fluxes for both the CK and ATP_{ase} reactions.

The $PCr \leftrightarrow ATP \leftrightarrow Pi$ exchange system in a normal brain likely reaches chemical equilibrium (or near equilibrium) under most circumstances. As long as the equilibrium condition is satisfied, one can further simplify the in vivo ^{31}P MT measurement procedure by using the chemical equilibrium relation (50). In this case, only two in vivo ^{31}P spectra (one control and another with full saturation of γ-ATP as illustrated in Fig. 15.11) are practically required to determine the entire $PCr \leftrightarrow ATP \leftrightarrow Pi$ exchange process (50). Thus, this simplification can make the in vivo ^{31}P MT measurement more robust for rapidly determining the ATP metabolic flux changes induced by either physiological or pathological perturbations.

5. Perspective and Discussion

Despite its low detection sensitivity compared to 1H MRS, researchers in the past three decades have revealed the great merits of in vivo heteronuclear MRS for a broad range of biomedical applications. Two of them (i.e., ^{31}P and ^{17}O) have been discussed here in great detail and each method provides a unique tool for noninvasively studying specific metabolic pathways in the brain through the measurements of metabolite concentrations and biochemical reaction fluxes. The combination of different in vivo multinuclear MRS approaches may significantly enhance the MR capability to perform comprehensive studies concerning brain physiology, neurochemistry, bioenergetics and their relations to brain function. This point is addressed by answering the following questions:

5.1. Why is in vivo ^{31}P MT Approach Attractive and Promising for Studying Brain Bioenergetics?

A large amount of research efforts have been spent since early 1980s for exploring the possibility of determining the ATP metabolic fluxes using a variety of in vivo 31P MRS MT approaches and great progress has been made (20, 44–46, 49, 50, 103–110, 115, 117). Nevertheless, the course for advancing the in vivo ^{31}P MRS MT methodology and its clinical application has been significantly slowed down particularly in brain studies during the last decade. One of the major causes is probably in regard to two controversial observations in this research field. The first one is the inconsistency in the results of the measured reverse ATP fluxes in the literature (e.g., (112–114)). In our opinion, this inconsistency is likely caused by the lack of comprehensive spin-exchange models used in

the early research work. And this controversy can be resolved by using more sophisticated three-spin exchange models for accurately determining the reverse ATP fluxes for both the CK and ATP_{ase} reactions (45,46,50,115,116).

Another surprising observation has raised question regarding whether the measured forward ATP_{ase} reaction flux truly reflects the oxidative phosphorylation in the mitochondria in a living organ. The ATP synthesis reaction (i.e., **R2** in Figs. 15.1 and 15.13) catalyzed by the coupled activities of glycolytic enzymes glyceraldehyde-3-phosphate dehydrogenase (GAPDH) and phosphoglycerate kinase (PGK) have been shown to be a major contributor to the $Pi \rightarrow ATP$ reaction flux measured by the ^{31}P MT approaches in E. coli (118), yeast (119), liver (120), and the myocardium (121). For instant, in the perfused rat heart, GAPDH/PGK mediated exchange dominates the $Pi \rightarrow ATP$ flux measured by the ^{31}P MT approach in the myocardium (121). Under these circumstances, *only if* the GAPDH/PGK effect was eliminated either directly using exogenous inhibitor iodoacetate or indirectly by eliminating all exogenous and endogenous sources of glucose, the myocardium $Pi \rightarrow ATP$ flux determined by the in vivo ^{31}P MRS MT measurement was found to be the same as the net rate of *oxidative* ATP synthesis calculated as the product of the cardiac oxygen consumption rate and the P:O ratio, and then the correlation between the measured flux and oxygen consumption rate became evident (121). These observations and findings reveal the complexity of biological systems and potential limitation of in vivo ^{31}P MRS MT approaches for directly measuring the ATP metabolic flux related to oxidative phosphorylation in some organs such as heart and liver. Interestingly, in contrast to the observations in the myocardium, and analogous observations in yeast, E. coli and liver, the $Pi \rightarrow ATP$ flux measured by in vivo ^{31}P MRS MT in the human brain is similar to the net oxidative ATP synthesis rate which can be estimated by the available $CMRO_2$ data and the P:O ratio based on a tight link between the cerebral oxidative phosphorylation and oxygen utilization under normal physiological condition (20, 50). The $CMRO_2$ value in the human occipital lobe has been measured to be 1.71 μmol/g/min by PET (91). The ATP synthesis rate attributed by oxidative phosphorylation can be calculated by multiplying this $CMRO_2$ value by the P:O ratio of ~2.5 (122) and factor of 2, resulting in an estimated value of 8.6 μmol/g/min. This rate is almost identical to the cerebral ATP synthesis rate of $F_f^{ATP_{ase}} = 8.8\ \mu\mathrm{mol}/g/min$, which was directly measured by in vivo ^{31}P MRS MT (50). A similar relation was also evident in the animal studies showing a tight correlation between the measured $Pi \rightarrow ATP$ flux and the estimated oxidative phosphor rate (49,123). These comparisons of results, thus, lead us to conclude that in the brain, the Pi→ATP flux measured by the in vivo ^{31}P MT approach equals the net oxidative ATP synthesis rate linking to the cerebral oxidative phosphorylation, and this flux should provide a vital index reflecting the major bioenergetics for supporting brain activity and function (7, 12, 20, 123). This conclusion makes in vivo ^{31}P MT attractive for studying the central role of the cerebral bioenergetics associated with oxidative phosphorylation and brain activity, though the underlying mechanism for explaining the discrepancy in the ^{31}P MT measurements between the brain and other organs (e.g., heart and liver) remains to be explored (20).

5.2. What Is the Possible Role that in vivo ^{31}P and ^{17}O MRS can Play for Studying Brain Activation and Function?

As mentioned earlier, both in vivo ^{31}P and ^{17}O MRS methods can provide noninvasive tools for studying brain metabolism and bioenergetics. Each of these methods has unique features for probing the metabolic functions in mitochondria. Specifically, the in vivo ^{17}O MRS imaging approach is useful for mapping the absolute $CMRO_2$ within a relatively short $^{17}O_2$ inhalation time. The $CMRO_2$ images should reflect the total metabolic rate of oxygen utilization (i.e., **R1** in Fig. 15.1) and its spatial distribution in the brain. In contrast, the in vivo ^{31}P MT approach is powerful for measuring all the cerebral ATP metabolic fluxes associated with four ATP reactions (i.e., **R2** to **R5** in Fig. 15.1) occurring in different subcellular compartments. All of these measured physiological parameters can be linked to brain ATP energy and ATP transportation. Therefore, the combination of in vivo ^{31}P and ^{17}O MRS methods may provide an essential in vivo MR tool being able to studying the crucial roles of both oxygen and ATP metabolisms in cerebral bioenergetics and brain functions.

One relevant question in the brain function and neuroimaging research fields is how much extra brain energy is needed during the brain stimulation and/or task performance. This topic is still in intense debate, especially regarding how much $CMRO_2$ is induced by brain stimulation (7, 8, 91, 124–136). A more important question, perhaps, is how many more ATP molecules are consumed during brain activation as compared to the resting brain because of a close relation between the ATP utilization and energy consumption (3, 7, 8). The answers to these questions are central for understanding the mechanisms underlying most modern neuroimaging techniques including two most popular methods of the functional MRI (fMRI) based on the blood oxygenation level dependent (BOLD) contrast (137–142) and PET (7,8,143). One major hurdle for addressing the questions is the lack of sophisticated and robust neuroimaging modalities for directly assessing the absolute $CMRO_2$ and CMR_{ATP}, which is equivalent to $F_{f\mathrm{ATP_{ase}}}$ in this article, and their changes elevated by brain activation. Therefore, the in vivo ^{31}P and ^{17}O MRS approaches as described here could fill this methodological gap and make significant contribution in understanding the relation between brain bioenergetics and function. This notion is convincingly supported by several lines of evidence provided by recent research progresses. One example of these progresses was to apply the in vivo ^{17}O MRS imaging approach for successfully mapping $CMRO_2$ images in the cat brain under resting and visual stimulation conditions (144). A significant $CMRO_2$ increase was observed in the activated cat visual cortex. This initial observation indicates the possible central role of oxygen metabolism for supporting the elevated brain activity during activation.

Another significant progress is related to the in vivo ^{31}P MT application in the rat brain for studying the quantitative correlation between the CMR_{ATP} and the varied brain activity from mild anesthesia state to the isoelectric state (123). In this study, we observed a strong correlation between the Pi→ATP flux measured by the in vivo ^{31}P MT approach and the brain activity quantified by EEG signal (123). This result indicates a tight correlation between the ATP synthesis rate and brain bioenergetic demand under varied brain activity states. Therefore, the measurement of Pi→ATP flux should provide a sensitive energy index for quantifying the brain bioenergetics. In contrast, the steady-state HEP concentrations

(e.g., [ATP], [PCr] and [Pi]) and pH are relatively stable in a wide range of brain activity level (123). These results support the view that one of the major functions of the $PCr \leftrightarrow ATP \leftrightarrow Pi$ exchange process is to sustain the balance between the ATP supply and demand in the brain resulting in a stable ATP concentration under the normal physiological condition. Such a balance is likely maintained by the rapid adjustments of both forward and reverse metabolic fluxes involved in the $PCr \leftrightarrow ATP \leftrightarrow Pi$ exchange according to the change of brain energy. We conclude that the ATP metabolic flux measurements using the in vivo ^{31}P MT approach should be more useful for studying the brain bioenergetic change in response to brain activation as compared to the steady-state HEP concentration measurements using conventional in vivo ^{31}P MRS. This is evident from two high-field in vivo ^{31}P MRS studies showing a few percents of decrease in the PCr signal in contrast to a >30% increase in the CK forward flux in the human visual cortex during visual stimulation (108, 145). It is conceivable that the in vivo ^{31}P MT approach, as a sole in vivo tool being able to directly and quantitatively measure the cerebral ATP metabolic fluxes, will play a vital role for studying the brain bioenergetics associated with brain function and activation. One particularly interesting question possibly to be addressed by this in vivo ^{31}P MT approach is whether more ATP utilization is required by the elevated neuronal activity, and if yes, how much more is needed? The answers should advance our understanding regarding the central roles of cerebral oxidative phosphorylation and mitochondria in supporting brain function.

5.3. What are the Potential Applications of in vivo ^{31}P and ^{17}O MRS for Clinical Research and Diagnosis?

In vivo MRS methodology can provide detailed metabolite fingerprints in the living organs, and it is perhaps one of the most classic molecular imaging modalities. Many metabolites and their abnormal changes, detectable by in vivo MRS, have been proved to be tightly linked to various brain diseases and disease progression.

Both of the in vivo ^{17}O MRS and ^{31}P MRS MT approaches as discussed here are especially useful for studying the brain oxidative metabolism and the mitochondrial metabolic function. They would provide opportunities for a variety of clinical brain research and potentially for clinical diagnosis because of the obvious role of oxidative metabolism in the pathology associated with many brain disorders and neurodegenerative diseases such as schizophrenia, Alzheimer’s disease, Huntington’s disease, Parkinson’s disease, mitochondrial dysfunction and aging problems (e.g., (146–150)). One line of evidence is the histopathological findings indicating that the activity of cytochrome oxidase, the key mitochondrial enzyme that catalyzes the reduction of oxygen to form water, is significantly impaired in schizophrenic (146) and Alzheimer’s patients (147, 148). Another line of evidence is from the studies of diseases caused by mitochondrial DNA mutations suggesting that a variety of degenerative processes in Parkinson’s disease and Alzheimer’s disease may be associated with defects in mitochondrial oxidative phosphorylation (151, 152). Thus, the in vivo ^{17}O MRS and ^{31}P MT approaches may play vital roles for investigating the neurodegenerative diseases associated with the mitochondrial abnormality and metabolic syndrome with great potential in clinical diagnosis and monitoring the brain functional recovery after medical treatment.

6. Conclusion

Although, in reality, in vivo heteronuclear MRS has not been widely applied compared to ^{1}H MRI/MRS due to its lower detection sensitivity, the currently available ultrahigh MRI/MRS scanners, technology and their associated high field merits have undoubtedly stimulated the in vivo heteronuclear MRS research and methodological development (153). Significant progresses have been made for advancing in vivo MRS in brain research. One of the unique in vivo MRS utilities is to noninvasively measure the cerebral metabolic fluxes and their dynamic changes, which may lead to many important applications in medical research. Two interesting and exciting applications of the in vivo ^{17}O MRS approach and/or ^{31}P MRS MT approach are: (i) to study the dynamic changes in oxygen utilization and oxidative ATP metabolism during activation in normal brains; (ii) to explore the possibility for detecting abnormality in the oxidative metabolic fluxes during the progression of brain diseases prior to showing metabolite concentration abnormality. The outcomes from these applications will be essential for better understanding of brain function and dysfunction. Finally, the in vivo ^{17}O and ^{31}P MRS can be readily combined with many other MRI utilities for imaging brain anatomy, perfusion, diffusion and BOLD etc within the same scanning session. This combined MRS/MRI strategy can make it particularly powerful in neuroscience research.

Acknowledgments

The authors would like to thank Drs. Hellmut Merkle, Run-Xia Tian, Peter Andersen, Gregor Adriany, Pete Thelwall and Mr. John Strupp for their technical assistance, support and scientific discussion. Part of the reviewed work was supported by NIH grants of NS41262, EB02632, NS39043, EB00329, P30NS057091 and P41 RR08079, the W.M. Keck Foundation and the MIND Institute.

References

1. Boyer PD. What makes ATP synthase spin? Nature. 1999; 402(6759):247, 249. [PubMed: 10580491]
2. Stock D, Leslie AG, Walker JE. Molecular architecture of the rotary motor in ATP synthase. Science. 1999; 286(5445):1700–1705. [PubMed: 10576729]
3. Siesjo, BK. Brain energy metabolism. New York: Wiley; 1978. p. 101-110.
4. Raichle, ME. Circulatory and metabolic correlates of brain function in normal humans. In: Mountcastle, VB.Plum, F., Geiger, SR., editors. Handbook of Physiology-The Nervous System. Bethesda: American Physiological Society; 1987. p. 643-674.
5. Clarke, DD., Sokoloff, L. Circulation and energy metabolism of the brain. In: Siegel, GJ., et al., editors. Basic Neruochemistry: Molecular, Cellular and Medical Aspects. Philadephia: Lippincott-Raven Publishers; 1999. p. 633-669.
6. Shulman RG, Rothman DL, Behar KL, Hyder F. Energetic basis of brain activity: Implications for neuroimaging. Trends Neurosci. 2004; 27(8):489–495. [PubMed: 15271497]
7. Hyder F, Patel AB, Gjedde A, Rothman DL, Behar KL, Shulman RG. Neuronal-glial glucose oxidation and glutamatergic-GABAergic function. J Cereb Blood Flow Metab. 2006; 26(7):865–877. [PubMed: 16407855]
8. Raichle ME, Mintun MA. Brain work and brain imaging. Annu Rev Neurosci. 2006; 29:449–476. [PubMed: 16776593]
9. Hevner RF, Wong-Riley MT. Regulation of cytochrome oxidase protein levels by functional activity in the macaque monkey visual system. J Neurosci. 1990; 10(4):1331–1340. [PubMed: 2158531]
10. Hevner RF, Duff RS, Wong-Riley MT. Coordination of ATP production and consumption in brain: Parallel regulation of cytochrome oxidase and Na^{+}, K^{+}-ATPase. Neurosci Lett. 1992; 138(1):188–192. [PubMed: 1328957]

11. Rolfe DF, Brown GC. Cellular energy utilization and molecular origin of standard metabolic rate in mammals. Physiol Rev. 1997; 77(3):731–758. [PubMed: 9234964]
12. Attwell D, Laughlin SB. An energy budget for signaling in the grey matter of the brain. J Cereb Blood Flow Metab. 2001; 21(10):1133–1145. [PubMed: 11598490]
13. Shulman RG, Rothman DL, Hyder F. Stimulated changes in localized cerebral energy consumption under anesthesia. Proc Natl Acad Sci USA. 1999; 96(6):3245–3250. [PubMed: 10077669]
14. Magistretti PJ, Pellerin L, Rothman DL, Shulman RG. Energy on demand. Science. 1999; 283(5401):496–497. [PubMed: 9988650]
15. Wallimann T, Hemmer W. Creatine kinase in non-muscle tissues and cells. Mol Cell Biochem. 1994; 133–134:193–220.
16. Saks VA, Ventura-Clapier R, Aliev MK. Metabolic control and metabolic capacity: Two aspects of creatine kinase functioning in the cells. Biochim Biophys Acta. 1996; 1274(3):81–88. [PubMed: 8664307]
17. Kemp GJ. Non-invasive methods for studying brain energy metabolism: what they show and what it means. Dev Neurosci. 2000; 22(5–6):418–428. [PubMed: 11111158]
18. Shulman RG, Brown TR, Ugurbil K, Ogawa S, Cohen SM, den Hollander JA. Cellular applications of ^{31}P and ^{13}C nuclear magnetic resonance. Science. 1979; 205(4402):160–166. [PubMed: 36664]
19. Ackerman JJH, Grove TH, Wong GG, Gadian DG, Radda GK. Mapping of metabolites in whole animals by ^{31}P NMR using surface coils. Nature. 1980; 283:167–170. [PubMed: 7350541]
20. Lei H, Ugurbil K, Chen W. Measurement of unidirectional Pi to ATP flux in human visual cortex at 7 Tesla using in vivo ^{31}P magnetic resonance spectroscopy. Proc Natl Acad Sci U S A. 2003; 100:14409–14414. [PubMed: 14612566]
21. Gadian DG, Williams SR, Bates TE, Kauppinen RA. NMR spectroscopy: current status and future possibilities. Acta Neurochir Suppl (Wien). 1993; 57:1–8. [PubMed: 8421944]
22. Weiner MW. NMR spectroscopy for clinical medicine. Animal models and clinical examples. Ann N Y Acad Sci. 1987; 508:287–299. [PubMed: 3326457]
23. Hossmann KA. Studies of experimental cerebral ischemia with NMR spectroscopy. Arzneimittelforschung. 1991; 41(3A):292–298. [PubMed: 1859498]
24. Lei H, Zhu XH, Zhang XL, Ugurbil K, Chen W. In vivo ^{31}P magnetic resonance spectroscopy of human brain at 7 T: An initial experience. Magn Reson Med. 2003; 49:199–205. [PubMed: 12541238]
25. Petroff OA, Prichard JW, Behar KL, Alger JR, den Hollander JA, Shulman RG. Cerebral intracellular pH by 31P nuclear magnetic resonance spectroscopy. Neurology. 1985; 35(6):781–788. [PubMed: 4000479]
26. Burt CT, Ribolow HJ. A hypothesis: Noncyclic phosphodiesters may play a role in membrane control. Biochem Med. 1984; 31(1):21–30. [PubMed: 6743296]
27. Burt CT, Ribolow H. Glycerol phosphorylcholine (GPC) and serine ethanolamine phosphodiester (SEP): Evolutionary mirrored metabolites and their potential metabolic roles. Comp Biochem Physiol Biochem Mol Biol. 1994; 108(1):11–20. [PubMed: 8205386]
28. Ross BM, Moszczynska A, Blusztajn JK, Sherwin A, Lozano A, Kish SJ. Phospholipid biosynthetic enzymes in human brain. Lipids. 1997; 32(4):351–358. [PubMed: 9113621]
29. Podo F. Tumour phospholipid metabolism. NMR Biomed. 1999; 12(7):413–439. [PubMed: 10654290]
30. Young RS, Chen B, Petroff OA, Gore JC, Cowan BE, Novotny EJ Jr, Wong M, Zuckerman K. The effect of diazepam on neonatal seizure: In vivo ^{31}P and ^{1}H NMR study. Pediatr Res. 1989; 25(1): 27–31. [PubMed: 2919113]
31. Welch KM, Levine SR, Martin G, Ordidge R, Vande Linde AM, Helpern JA. Magnetic resonance spectroscopy in cerebral ischemia. Neurol Clin. 1992; 10(1):1–29.
32. Duncan JS. Imaging and epilepsy. Brain. 1997; 120(Pt 2):339–377. [PubMed: 9117380]
33. Hetherington HP, Pan JW, Spencer DD. ^{1}H and ^{31}P spectroscopy and bioenergetics in the lateralization of seizures in temporal lobe epilepsy. J Magn Reson Imaging. 2002; 16(4):477–483. [PubMed: 12353261]

34. Brown GG, Levine SR, Gorell JM, Pettegrew JW, Gdowski JW, Bueri JA, Helpern JA, Welch KM. In vivo ^{31}P NMR profiles of Alzheimer's disease and multiple subcortical infarct dementia. Neurology. 1989; 39(11):1423–1427. [PubMed: 2812317]
35. Pettegrew JW, Klunk WE, Panchalingam K, McClure RJ, Stanley JA. Magnetic resonance spectroscopic changes in Alzheimer's disease. Ann N Y Acad Sci. 1997; 826:282–306. [PubMed: 9329700]
36. Riehemann S, Volz HP, Smesny S, Hubner G, Wenda B, Rossger G, Sauer H. Phosphorus 31 magnetic resonance spectroscopy in schizophrenia research. Pathophysiology of cerebral metabolism of high-energy phosphate and membrane phospholipids. Nervenarzt. 2000; 71(5):354–363. [PubMed: 10846710]
37. Jensen JE, Al-Semaan YM, Williamson PC, Neufeld RW, Menon RS, Schaeffer B, Dens-more M, Drost DJ. Region-specific changes in phospholipid metabolism in chronic, medicated schizophrenia: ^{31}P-MRS study at 4.0 Tesla. Br J Psychiatry. 2002; 180:39–44. [PubMed: 11772850]
38. Ramadan NM, Halvorson H, Vande-Linde A, Levine SR, Helpern JA, Welch KM. Low brain magnesium in migraine. Headache. 1989; 29(9):590–593. [PubMed: 2584000]
39. Altura BM, Altura BT. Role of magnesium and calcium in alcohol-induced hypertension and strokes as probed by in vivo television microscopy, digital image microscopy, optical spectroscopy, 31P-NMR, spectroscopy and a unique magnesium ion-selective electrode. Alcohol Clin Exp Res. 1994; 18(5):1057–1068. [PubMed: 7847586]
40. Nioka S, Zaman A, Yoshioka H, Masumura M, Miyake H, Lockard S, Chance B. ^{31}P magnetic resonance spectroscopy study of cerebral metabolism in developing dog brain and its relationship to neuronal function. Dev Neurosci. 1991; 13(2):61–68. [PubMed: 1649043]
41. Nioka S, Smith DS, Mayevsky A, Dobson GP, Veech RL, Subramanian H, Chance B. Age dependence of steady state mitochondrial oxidative metabolism in the in vivo hypoxic dog brain. Neurol Res. 1991; 13(1):25–32. [PubMed: 1675443]
42. Chance B, Leigh JS Jr, Nioka S, Sinwell T, Younkin D, Smith DS. An approach to the problem of metabolic heterogeneity in brain: Ischemia and reflow after ischemia. Ann N Y Acad Sci. 1987; 508:309–320. [PubMed: 3439706]
43. Frosen S, Hoffman RA. Study of moderately rapid chemical exchange by means of nuclear magnetic double resonance. J Chem Phys. 1963; 39:2892–2901.
44. Alger JR, Shulman RG. NMR Studies of enzymatic rates in vitro and in vivo by magnetization transfer. Quart Rev Biophys. 1984; 17:83–124.
45. Ugurbil K. Magnetization transfer measurements of individual rate constants in the presence of multiple reactions. J Magn Reson. 1985; 64:207–219.
46. Ugurbil K. Magnetization transfer measurements of creatine kinase and ATPase rates in intact hearts. Circulation. 1985; 72:IV94–IV96. [PubMed: 2932267]
47. Degani H, Laughlin M, Campbell S, Shulman RG. Kinetics of creatine kinase in heart: a ^{31}P NMR saturation- and inversion-transfer study. Biochemistry. 1985; 24(20):5510–5516. [PubMed: 4074712]
48. Bottomley PA, Ouwerkerk R, Lee RF, Weiss RG. Four-angle saturation transfer (FAST) method for measuring creatine kinase reaction rates in vivo. Magn Reson Med. 2002; 47(5):850–863. [PubMed: 11979563]
49. Shoubridge EA, Briggs RW, Radda GK. ^{31}P NMR saturation transfer measurements of the steady state rates of creatine kinase and ATP synthetase in the rat brain. FEBS Lett. 1982; 140(2):289–292. [PubMed: 6282642]
50. Du F, Zhu XH, Qiao H, Zhang X, Chen W. Efficient in vivo ^{31}P magnetization transfer approach for noninvasively determining multiple kinetic parameters and metabolic fluxes of ATP metabolism in the human brain. Magn Reson Med. 2006; 57(1):103–114.
51. Mateescu, GD., Yvars, GM., Dular, T. Water, Ions and O-17 Magnetic Resonance Imaging. In: Lauger, P.Packer, L., Vasilescu, V., editors. Water and Ions in Biological Systems. Basel-Boston-Berlin: Birkhauser Verlag; 1988. p. 239-250.

52. Pekar J, Ligeti L, Ruttner Z, Lyon RC, Sinnwell TM, van Gelderen P, Fiat D, Moonen CT, McLaughlin AC. In vivo measurement of cerebral oxygen consumption and blood flow using ^{17}O magnetic resonance imaging. Magn Reson Med. 1991; 21(2):313–319. [PubMed: 1745131]
53. Fiat D, Ligeti L, Lyon RC, Ruttner Z, Pekar J, Moonen CT, McLaughlin AC. In vivo ^{17}O NMR study of rat brain during $^{17}O_2$ inhalation. Magn Reson Med. 1992; 24(2):370–374. [PubMed: 1569875]
54. Zhu XH, Zhang Y, Tian RX, Lei H, Zhang N, Zhang X, Merkle H, Ugurbil K, Chen W. Development of ^{17}O NMR approach for fast imaging of cerebral metabolic rate of oxygen in rat brain at high field. Proc Natl Acad Sci U S A. 2002; 99(20):13194–13199. [PubMed: 12242341]
55. Zhu XH, Zhang N, Zhang Y, Zhang X, Ugurbil K, Chen W. In vivo ^{17}O NMR approaches for brain study at high field. NMR Biomed. 2005; 18(2):83–103. [PubMed: 15770611]
56. Ernst, RR., Bodenhausen, G., Wokaun, A. Principles of Nuclear Magnetic Resonance in One and Two Dimensions. New York: Oxford University Press; 1991.
57. Hoult DI, Richards RE. The signal-to-noise ratio of nuclear magnetic resonance experiment. J Magn Reson. 1976; 24:71–85.
58. Wen H, Chesnick AS, Balaban RS. The design and test of a new volume coil for high field imaging. Magn Reson Med. 1994; 32:492–498. [PubMed: 7997115]
59. Wang Z, Wang DJ, Noyszewski EA, Bogdan AR, Haselgrove JC, Reddy R, Zimmerman RA, Leigh JS. Sensitivity of in vivo MRS of the N-δ proton in proximal histidine of deoxymyoglobin. Magn Reson Med. 1992; 27(2):362–367. [PubMed: 1334205]
60. Qiao H, Zhang X, Zhu XH, Du F, Chen W. In vivo ^{31}P MRS of human brain at high/ultrahigh fields: A quantitative comparison of NMR detection sensitivity and spectral resolution between 4 T and 7 T. Magn Reson Imaging. 2006; 24(10):1281–1286. [PubMed: 17145398]
61. Boska MD, Hubesch B, Meyerhoff DJ, Twieg DB, Karczmar GS, Matson GB, Weiner MW. Comparison of ^{31}P MRS and ^{1}H MRI at 1.5 and 2.0 T. Magn Reson Med. 1990; 13(2):228–238. [PubMed: 2314213]
62. Hardy CJ, Bottomley PA, Roemer PB, Redington RW. Rapid ^{31}P spectroscopy on a 4-T whole-body system. Magn Reson Med. 1988; 8(1):104–109. [PubMed: 3173064]
63. Hetherington HP, Spencer DD, Vaughan JT, Pan JW. Quantitative ^{31}P spectroscopic imaging of human brain at 4 Tesla: assessment of gray and white matter differences of phosphocreatine and ATP. Magn Reson Med. 2001; 45:46–52. [PubMed: 11146485]
64. Evelhoch JL, Ewy CS, Siegfried BA, Ackerman JJ, Rice DW, Briggs RW. ^{31}P spin-lattice relaxation times and resonance linewidths of rat tissue in vivo: Dependence upon the static magnetic field strength. Magn Reson Med. 1985; 2(4):410–417. [PubMed: 4094555]
65. Mathur-De Vre R, Maerschalk C, Delporte C. Spin-lattice relaxation times and nuclear Overhauser enhancement effect for ^{31}P metabolites in model solutions at two frequencies: Implications for in vivo spectroscopy. Magn Reson Imaging. 1990; 8(6):691–698. [PubMed: 2266794]
66. Abragam, A. The Principles of Nuclear Magnetism. Mott, NF.Bullard, EC., Wilkinson, DH., editors. London: Oxford University Press; 1961.
67. Zhu XH, Merkle H, Kwag JH, Ugurbil K, Chen W. ^{17}O relaxation time and NMR sensitivity of cerebral water and their field dependence. Magn Reson Med. 2001; 45(4):543–549. [PubMed: 11283979]
68. Thelwall, PE., Blackband, SJ., Chen, W. Proc Intl Soc Mag Reson Med (ISMRM). Toronto: 2003. Field dependence of ^{17}O T_1, T_2 and SNR – in vitro and in vivo studies at 4.7, 11 and 17.6 Tesla; p. 504
69. Mateescu, GD., Yvars, G., Pazara, DI., Alldridge, NA., LaManna, JC., Lust, DW., Mattingly, M., Kuhn, W. ^{17}O-^{1}H magnetic resonance imaging in plants, animals, and materials. In: Baillie, TA., Jones, JR., editors. Synthesis and Application of Isotopically Labeled Compounds. Amsterdam: Elsevier; 1989. p. 499-508.
70. Hopkins AL, Barr RG. Oxygen-17 compounds as potential NMR T_2 contrast agents: Enrichment effects of H_2 ^{17}O on protein solutions and living tissues. Magn Reson Med. 1987; 4(4):399–403. [PubMed: 3586987]

71. Kwong KK, Hopkins AL, Belliveau JW, Chesler DA, Porkka LM, McKinstry RC, Finelli DA, Hunter GJ, Moore JB, Barr RG, Rosen BR. Proton NMR imaging of cerebral blood flow using $H_2{}^{17}O$. Magn Reson Med. 1991; 22(1):154–158. [PubMed: 1798389]
72. Arai T, Nakao S, Mori K, Ishimori K, Morishima I, Miyazawa T, Fritz-Zieroth B. Cerebral oxygen utilization analyzed by the use of oxygen-17 and its nuclear magnetic resonance. Biochem Biophys Res Commun. 1990; 169(1):153–158. [PubMed: 2350339]
73. Pekar J, Sinnwell T, Ligeti L, Chesnick AS, Frank JA, McLaughlin AC. Simultaneous measurement of cerebral oxygen consumption and blood flow using ^{17}O and ^{19}F magnetic resonance imaging. J Cereb Blood Flow Metab. 1995; 15(2):312–320. [PubMed: 7860664]
74. Ronen I, Navon G. A new method for proton detection of $H_2{}^{17}O$ with potential applications for functional MRI. Magn Reson Med. 1994; 32(6):789–793. [PubMed: 7869903]
75. Ronen I, Merkle H, Ugurbil K, Navon G. Imaging of $H_2{}^{17}O$ distribution in the brain of a live rat by using proton-detected ^{17}O MRI. Proc Natl Acad Sci U S A. 1998; 95(22):12934–12939. [PubMed: 9789018]
76. Reddy R, Stolpen AH, Leigh JS. Detection of ^{17}O by proton T_1 rho dispersion imaging. J Magn Reson B. 1995; 108(3):276–279. [PubMed: 7670758]
77. Chen, W., Zhu, XH., Ugurbil, K. Imaging cerebral metabolic rate of oxygen consumption ($CMRO_2$) using ^{17}O NMR approach at ultra-high field. In: Shulman, RG., Rothman, DL., editors. Brain Energetics and Neuronal Activity. New York: John Wiley & Sons Ltd; 2004. p. 125-146.
78. Arai T, Mori K, Nakao S, Watanabe K, Kito K, Aoki M, Mori H, Morikawa S, Inubushi T. In vivo oxygen-17 nuclear magnetic resonance for the estimation of cerebral blood flow and oxygen consumption. Biochem Biophys Res Commun. 1991; 179(2):954–961. [PubMed: 1898415]
79. Fiat D, Kang S. Determination of the rate of cerebral oxygen consumption and regional cerebral blood flow by non-invasive ^{17}O in vivo NMR spectroscopy and magnetic resonance imaging: Part 1. Theory and data analysis methods. Neurol Res. 1992; 14(4):303–311. [PubMed: 1360624]
80. Fiat D, Dolinsek J, Hankiewicz J, Dujovny M, Ausman J. Determination of regional cerebral oxygen consumption in the human: ^{17}O natural abundance cerebral magnetic resonance imaging and spectroscopy in a whole body system. Neurol Res. 1993; 15(4):237–248. [PubMed: 8105403]
81. Fiat D, Kang S. Determination of the rate of cerebral oxygen consumption and regional cerebral blood flow by non-invasive ^{17}O in vivo NMR spectroscopy and magnetic resonance imaging. Part 2. Determination of $CMRO_2$ for the rat by ^{17}O NMR, and $CMRO_2$, rCBF and the partition coefficient for the cat by ^{17}O MRI. Neurol Res. 1993; 15(1):7–22. [PubMed: 8098859]
82. Mateescu GD. Functional oxygen-17 magnetic resonance imaging and localized spectroscopy. Adv Exp Med Biol. 2003; 510:213–218. [PubMed: 12580430]
83. Stolpen AH, Reddy R, Leigh JS. ^{17}O-decoupled proton MR spectroscopy and imaging in a tissue model. J Magn Reson. 1997; 125(1):1–7. [PubMed: 9245354]
84. Reddy R, Stolpen AH, Charagundla SR, Insko EK, Leigh JS. ^{17}O-decoupled 1H detection using a double-tuned coil. Magn Reson Imaging. 1996; 14(9):1073–1078. [PubMed: 9070998]
85. de Crespigny AJ, D'Arceuil HE, Engel-horn T, Moseley ME. MRI of focal cerebral ischemia using ^{17}O-labeled water. Magn Reson Med. 2000; 43(6):876–883. [PubMed: 10861883]
86. Zhu XH, Zhang Y, Zhang N, Ugurbil K, Chen W. Noninvasive and three-dimensional imaging of $CMRO_2$ in rats at 9.4 T: Reproducibility test and normothermia/hypothermia comparison study. J Cereb Blood Flow Metab. 2007; 27(6):1225–1234. [PubMed: 17133228]
87. Zhang N, Zhu XH, Lei H, Ugurbil K, Chen W. Simplified methods for calculating cerebral metabolic rate of oxygen based on ^{17}O magnetic resonance spectroscopic imaging measurement during a short $^{17}O_2$ inhalation. J Cereb Blood Flow Metab. 2004; 24(8):840–848. [PubMed: 15362714]
88. Ter-Pogossian MM, Eichling JO, Davis DO, Welch MJ. The measure in vivo of regional cerebral oxygen utilization by means of oxyhemoglobin labeled with radioactive oxygen-15. J Clin Invest. 1970; 49:381–391. [PubMed: 5411789]
89. Lenzi GL, Jones T, Frackowiak RS. Positron emission tomography: state of the art in neurology. Prog Nucl Med. 1981; 7:118–137. [PubMed: 6976591]

90. Mintun MA, Raichle ME, Martin WR, Herscovitch P. Brain oxygen utilization measured with O-15 radiotracers and positron emission tomography. J Nucl Med. 1984; 25(2):177–187. [PubMed: 6610032]
91. Fox PT, Raichle ME, Mintun MA, Dence C. Nonoxidative glucose consumption during focal physiologic neural activity. Science. 1988; 241:462–464. [PubMed: 3260686]
92. Kety SS, Schmidt CF. The determination of cerebral blood flow in man by the use of nitrous oxide in low concentrations. Am J Physiol. 1945; 143:53–66.
93. Kety SS, Schmidt CF. Nitrous oxide method for the quantitative determination of cerebral blood flow in man: theory, procedure and normal values. J Clin Invest. 1948; 27:476–483. [PubMed: 16695568]
94. Kety SS, Schmidt CF. Effects of altered arterial tensions of carbon dioxide and oxygen on cerebral blood flow and cerebral oxygen consumption of normal young men. J Clin Invest. 1948; 27:484–492. [PubMed: 16695569]
95. Herscovitch A, Raichle ME. What is the correct value for the brain-blood partition coefficient for water? J Cereb Blood Flow Metab. 1985; 5:65–69. [PubMed: 3871783]
96. Herscovitch P, Raichle ME, Kilbourn MR, Welch MJ. Positron emission tomographic measurement of cerebral blood flow and permeability-surface area product of water using [15O]water and [11C]butanol. J Cereb Blood Flow Metab. 1987; 7(5):527–542. [PubMed: 3498732]
97. Zhang X, Zhu XH, Tian R, Zhang Y, Merkle H, Chen W. Measurement of arterial input function of ^{17}O water tracer in rat carotid artery by using a region-defined (REDE) implanted vascular RF coil. Magma. 2003; 16(2):77–85. [PubMed: 12845538]
98. Nakao Y, Itoh Y, Kuang TY, Cook M, Jehle J, Sokoloff L. Effects of anesthesia on functional activation of cerebral blood flow and metabolism. Proc Natl Acad Sci U S A. 2001; 98(13):7593–7598. [PubMed: 11390971]
99. Hyder F, Kennan RP, Kida I, Mason GF, Behar KL, Rothman D. Dependence of oxygen delivery on blood flow in rat brain: A 7 tesla nuclear magnetic resonance study. J Cereb Blood Flow Metab. 2000; 20(3):485–498. [PubMed: 10724113]
100. Yee SH, Lee K, Jerabek PA, Fox PT. Quantitative measurement of oxygen metabolic rate in the rat brain using microPET imaging of briefly inhaled ^{15}O-labelled oxygen gas. Nucl Med Commun. 2006; 27(7):573–581. [PubMed: 16794518]
101. Zhang, NY., Zhu, XH., Chen, W. Proc Intl Soc Mag Reson Med (ISMRM). Seattle: 2006. Evaluation of the simplified method for mapping cerebral metabolic rate of oxygen based on ^{17}O NMR approach; p. 952
102. Erecinska M, Thoresen M, Silver IA. Effects of hypothermia on energy metabolism in Mammalian central nervous system. J Cereb Blood Flow Metab. 2003; 23(5):513–530. [PubMed: 12771566]
103. Weiss RG, Gerstenblith G, Bottomley PA. ATP flux through creatine kinase in the normal, stressed, and failing human heart. Proc Natl Acad Sci U S A. 2005; 102(3):808–813. [PubMed: 15647364]
104. Balaban RS, Kantor HL, Ferretti JA. In vivo flux between phosphocreatine and adenosine triphosphate determined by two-dimensional phosphorous NMR. J Biol Chem. 1983; 258(21): 12787–12789. [PubMed: 6630206]
105. Degani H, Alger JR, Shulman RG, Petroff OA, Prichard JW. ^{31}P magnetization transfer studies of creatine kinase kinetics in living rabbit brain. Magn Reson Med. 1987; 5(1):1–12. [PubMed: 3657491]
106. Bottomley PA, Hardy CJ. Mapping creatine kinase reaction rates in human brain and heart with 4 Tesla saturation transfer ^{31}P NMR. J Magn Reson. 1992; 99:443–448.
107. Sauter A, Rudin M. Determination of creatine kinase parameters in rat brain by NMR magnetization transfer. J Biological Chem. 1993; 268:13166–13171.
108. Chen W, Zhu X-H, Adriany G, Ugurbil K. Increase of creatine kinase activity in the visual cortex of human brain during visual stimulation: A ^{31}P NMR magnetization transfer study. Magn Reson Med. 1997; 38:551–557. [PubMed: 9324321]

109. Braunova Z, Kasparova S, Mlynarik V, Mierisova S, Liptaj T, Tkac I, Gvozdjakova A. Metabolic changes in rat brain after prolonged ethanol consumption measured by 1H and 31P MRS experiments. Cell Mol Neurobiol. 2000; 20(6):703–715. [PubMed: 11100978]

110. Mlynarik v ZS, Brehm A, Bischof M, Roden M. An optimized protocol for measuring rate constant of creatine kinase reaction in human brain by ^{31}P NMR saturation transfer. 13th Proc Intl Soc Mag Reson Med. 2005:2767.

111. Joubert F, Mateo P, Gillet B, Beloeil JC, Mazet JL, Hoerter JA. CK flux or direct ATP transfer: Versatility of energy transfer pathways evidenced by NMR in the perfused heart. Mol Cell Biochem. 2004; 256–257(1–2):43–58.

112. Matthews PM, Bland JL, Gadian DG, Radda GK. A ^{31}P-NMR saturation transfer study of the regulation of creatine kinase in the rat heart. Biochim Biophys Acta. 1982; 721(3):312–320. [PubMed: 7171631]

113. Mora BN, Narasimhan PT, Ross BD. ^{31}P magnetization transfer studies in the monkey brain. Magn Reson Med. 1992; 26(1):100–115. [PubMed: 1625557]

114. Bittl JA, DeLayre J, Ingwall JS. Rate equation for creatine kinase predicts the in vivo reaction velocity: ^{31}P NMR surface coil studies in brain, heart, and skeletal muscle of the living rat. Biochemistry. 1987; 26:6083–6090. [PubMed: 3689762]

115. Ugurbil K, Petein M, Maiden R, Michurski S, From A. Measurement of an individual rate constant in the presence of multiple exchanges: Application to myocardial creatine kinase rates. Biochemistry. 1986; 25:100–108. [PubMed: 3954984]

116. Spencer RG, Balschi JA, Leigh JS Jr, Ingwall JS. ATP synthesis and degradation rates in the perfused rat heart. 31P-nuclear magnetic resonance double saturation transfer measurements. Biophys J. 1988; 54(5):921–929. [PubMed: 3242635]

117. Joubert F, Mazet JL, Mateo P, Hoerter JA. ^{31}P NMR detection of subcellular creatine kinase fluxes in the perfused rat heart: Contractility modifies energy transfer pathways. J Biol Chem. 2002; 277(21):18469–18476. [PubMed: 11886866]

118. Mitsumori F, Rees D, Brindle KM, Radda GK, Campbell ID. ^{31}P-NMR saturation transfer studies of aerobic Escherichia coli cells. Biochimica et Biophysica Acta. 1988; 969(2):185–193. [PubMed: 2895671]

119. Campbell SL, Jones KA, Shulman RG. ^{31}P NMR saturation-transfer measurements in Saccharomyces cerevisiae: Characterization of phosphate exchange reactions by iodoacetate and antimycin A inhibition. Biochemistry. 1987; 26(23):7483–7492. [PubMed: 3322400]

120. Thoma WJ, Ugurbil K. Saturation-transfer studies of ATP-Pi exchange in isolated perfused rat liver. Biochimica et Biophysica Acta. 1987; 893(2):225–231. [PubMed: 2887203]

121. Kingsley-Hickman PB, Sako EY, Mohanakrishnan P, Robitaille PM, From AH, Foker JE, Ugurbil K. ^{31}P NMR studies of ATP synthesis and hydrolysis kinetics in the intact myocardium. Biochemistry. 1987; 26(23):7501–7510. [PubMed: 3427090]

122. Hinkle PC. P/O ratios of mitochondrial oxidative phosphorylation. Biochim Biophys Acta. 2005; 1706(1–2):1–11. [PubMed: 15620362]

123. Du, F., Zhang, Y., Friedman, M., Zhu, XH., Ugurbil, K., Chen, W. Proc Intl Soc Mag Reson Med (ISMRM). Seattle: 2006. Study of correlation between brain activity and ATP metabolic rates by means of ^{31}P magnetization transfer and electroencephalograph measurement; p. 2125

124. Fox PT, Raichle ME. Focal physiological uncoupling of cerebral blood flow and oxidative metabolism during somatosensory stimulation in human subjects. Proc Natl Acad Sci USA. 1986; 83:1140–1144. [PubMed: 3485282]

125. Ribeiro, L., Kuwabara, H., Meyer, E., Fujita, H., Marrett, S., Evans, A., Gjedde, A. Cerebral blood flow and metabolism during nonspecific bilateral visual stimulation in normal subjects. In: Uemura, K., editor. Quantification of Brain Function in Tracer Kinetics and Image Analysis in Brain PET. New York: Elsevier Science; 1993. p. 229-236.

126. Roland PE, Ericksson L, Stone-Elander S, Widen L. Does mental activity change the oxidative metabolism of the brain? J Neurosci. 1987; 7:2373–2389. [PubMed: 3612246]

127. Marrett, S., Fujita, H., Meyer, E., Ribeiro, L., Evans, A., Kuwabara, H., Gjedde, A. Stimulus specific increase of oxidative metabolism in human visual cortex. In: Uemura, K., editor.

Quantification of Brain Function in Tracer Kinetics and Image Analysis in Brain PET. New York: Elsevier Science; 1993. p. 217-228.

128. Prichard J, Rothman D, Novotny E, Petroff O, Kuwabara T, Avison M, Howseman A, Hanstock C, Shulman RG. Lactate rise detected by ^{1}H NMR in human visual cortex during physiologic stimulation. Proc Natl Acad Sci (USA). 1992; 88:5829–5831.
129. Shulman RG, Hyder F, Rothman DL. Cerebral energetics and the glycogen shunt: neurochemical basis of functional imaging. Proc Natl Acad Sci U S A. 2001; 98(11):6417–6422. [PubMed: 11344262]
130. Vafaee MS, Meyer E, Marrett S, Paus T, Evans AC, Gjedde A. Frequency-dependent changes in cerebral metabolic rate of oxygen during activation of human visual cortex. J Cereb Blood Flow Metab. 1999; 19(3):272–277. [PubMed: 10078879]
131. Davis TL, Kwong KK, Weisskoff RM, Rosen BR. Calibrated functional MRI: Mapping the dynamic of oxidative metabolism. Proc Natl Acad Sci USA. 1998; 95:1834–1839. [PubMed: 9465103]
132. Hoge RD, Atkinson J, Gill B, Crelier GR, Marrett S, Pike GB. Investigation of BOLD signal dependence on cerebral blood flow and oxygen consumption: The deoxyhemoglobin dilution model [In Process Citation]. Magn Reson Med. 1999; 42(5):849–863. [PubMed: 10542343]
133. Hyder F, Chase JR, Behar KL, Mason GF, Siddeek M, Rothman DL, Shulman RG. Increase tricarboxylic acid cycle flux in rat brain during forepaw stimulation detected with ^{1}H-{^{13}C} NMR. Proc Natl Acad Sci USA. 1996; 93:7612–7617. [PubMed: 8755523]
134. Kim SG, Rostrup E, Larsson HB, Ogawa S, Paulson OB. Determination of relative CMRO2 from CBF and BOLD changes: Significant increase of oxygen consumption rate during visual stimulation. Magn Reson Med. 1999; 41(6):1152–1161. [PubMed: 10371447]
135. Chen W, Zhu XH, Gruetter R, Seaquist ER, Ugurbil K. Study of oxygen utilization changes of human visual cortex during hemifield stimulation using ^{1}H-{^{13}C} MRS and fMRI. Magn Reson Med. 2001; 45:349–355. [PubMed: 11241689]
136. Kasischke KA, Vishwasrao HD, Fisher PJ, Zipfel WR, Webb WW. Neural activity triggers neuronal oxidative metabolism followed by astrocytic glycolysis. Science. 2004; 305(5680):99–103. [PubMed: 15232110]
137. Ogawa S, Lee T-M, Kay AR, Tank DW. Brain magnetic resonance imaging with contrast dependent on blood oxygenation. Proc Natl Acad Sci USA. 1990; 87:9868–9872. [PubMed: 2124706]
138. Ogawa S, Tank DW, Menon R, Ellermann JM, Kim S-G, Merkle H, Ugurbil K. Intrinsic signal changes accompanying sensory stimulation: Functional brain mapping with magnetic resonance imaging. Proc Natl Acad Sci USA. 1992; 89:5951–5955. [PubMed: 1631079]
139. Kwong KK, Belliveau JW, Chesler DA, Goldberg IE, Weisskoff RM, Poncelet BP, Kennedy DN, Hoppel BE, Cohen MS, Turner R, Cheng HM, Brady TJ, Rosen BR. Dynamic magnetic resonance imaging of human brain activity during primary sensory stimulation. Proc Natl Acad Sci USA. 1992; 89:5675–5679. [PubMed: 1608978]
140. Bandettini PA, Wong EC, Hinks RS, Tikofsky RS, Hyde JS. Time course EPI of human brain function during task activation. Magn Reson Med. 1992; 25:390–397. [PubMed: 1614324]
141. Frahm J, Bruhn H, Merboldt KD, Han-icke W. Dynamic MR imaging of human brain oxygenation during rest and photic stimulation. J Magn Reson Imag. 1992; 2(5):501–505.
142. Blamire AM, Ogawa S, Ugurbil K, Rothman D, McCarthy G, Ellermann JM, Hyder F, Rattner Z, Shulman RG. Dynamic mapping of the human visual cortex by high-speed magnetic resonance imaging. Proc Natl Acad Sci USA. 1992; 89:11069–11073. [PubMed: 1438317]
143. Barinaga M. What makes brain neurons run. Science. 1997; 276:196–198. [PubMed: 9132940]
144. Zhu, XH., Zhang, Y., Zhang, NY., Zhang, XL., Ugurbil, K., Chen, W. Proc Intl Soc Mag Reson Med (ISMRM). Seattle: 2006. Direct imaging of $CMRO_2$ in cat visual cortex at rest and visual stimulation; p. 457
145. Lei, H., Zhu, XH., Li, YX., Ugurbil, K., Chen, W. Proc Intl Soc Mag Reson Med (ISMRM). Kyoto, Japan: 2004. Changes of cerebral metabolism in human primary visual cortex during functional activation observed by in vivo ^{31}P MRS at 7T; p. 2361

146. Maurer I, Zierz S, Moller H. Evidence for a mitochondrial oxidative phosphorylation defect in brains from patients with schizophrenia. Schizophr Res. 2001; 48(1):125–136. [PubMed: 11278159]

147. Wong-Riley M, Antuono P, Ho KC, Egan R, Hevner R, Liebl W, Huang Z, Rachel R, Jones J. Cytochrome oxidase in Alzheimer's disease: Biochemical, histochemical, and immunohistochemical analyses of the visual and other systems. Vision Res. 1997; 37(24):3593–3608. [PubMed: 9425533]

148. Maurer I, Zierz S, Moller HJ. A selective defect of cytochrome c oxidase is present in brain of Alzheimer disease patients. Neurobiol Aging. 2000; 21(3):455–462. [PubMed: 10858595]

149. Frackowiak RS, Herold S, Petty RK, Morgan-Hughes JA. The cerebral metabolism of glucose and oxygen measured with positron tomography in patients with mitochondrial diseases. Brain. 1988; 111(Pt 5):1009–1024. [PubMed: 3263167]

150. Beal MF. Does impairment of energy metabolism result in excitotoxic neuronal death in neurodegenerative illnesses? Ann Neurol. 1992; 31(2):119–130. [PubMed: 1349466]

151. Wallace DC. Mitochondrial genetics: A paradigm for aging and degenerative diseases? Science. 1992; 256(5057):628–632. [PubMed: 1533953]

152. Wallace DC. Mitochondrial diseases in man and mouse. Science. 1999; 283(5407):1482–1488. [PubMed: 10066162]

153. Ugurbil, K., Adriany, G., Akgün, C., Andersen, P., Chen, W., Garwood, M., Gruetter, R., Henry, P-G., Marjanska, M., Moeller, S., Van de Moortele, P-F., Prüssmann, K., Tkac, I., Vaughan, JT., Wiesinger, F., Yacoub, E., Zhu, X-H. High Magnetic Fields for Imaging Cerebral Morphology, Function and Biochemistry. In: Robitaille, PMLaB LJ., editor. Biological Magnetic Resonance: Ultra High Field Magnetic Resonance Imaging Volume 26. New York: Springer; 2006. p. 285-342.

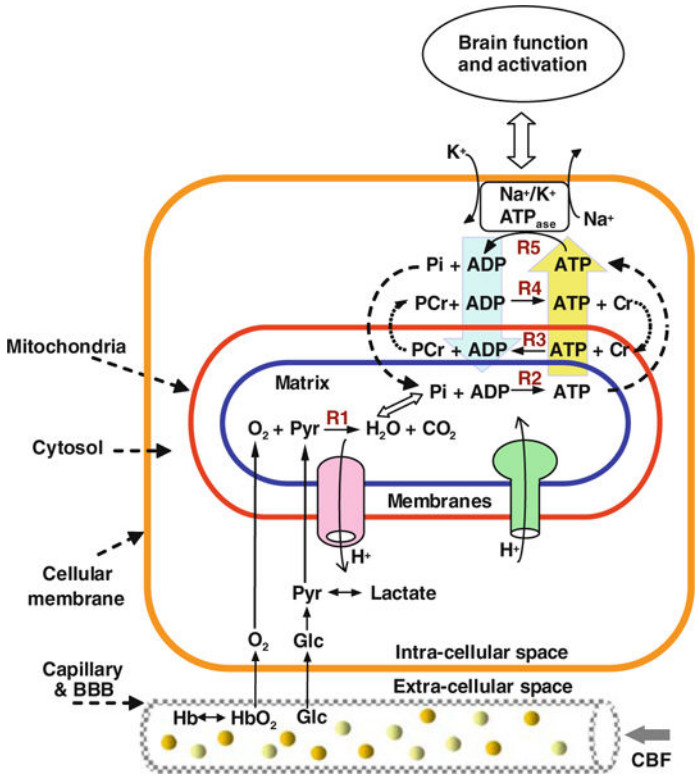

Fig. 15.1.

Schematic diagram of simplified major brain network involving metabolisms and hemodynamics occurring in the capillary, subcellular compartments including the mitochondria and cytosol spaces. Oxygen dissociates from hemoglobin (Hb) and enters mitochondria and it is metabolized with pyruvate (Pyr) which is converted from glucose (Glc). This oxygen utilization via Reaction 1 (R1) is tightly coupled with four ATP reactions for generating ATP (R2), consuming ATP (R5), transporting and buffering ATP energy via the paired CK reactions (R3 vs. V4). These four ATP reactions constitute a chemical exchange network *PCr↔ATP↔Pi*. This neurovascular-metabolic coupled network is essential for brain function.

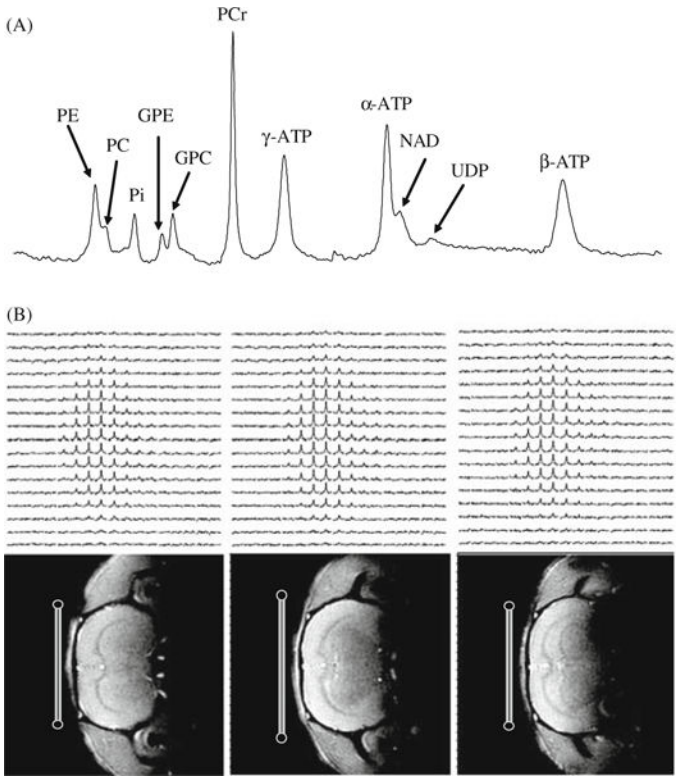

Fig. 15.2.

(**A**) A typical ^{31}P MR spectra acquired from the human occipital lobe at 7T with a total sampling time of 6.4 minutes. The spectrum is characterized by excellent spectral resolution and NMR sensitivity, and a large number of well-resolved resonance peaks from phosphoethanolamine (PE); phosphocholine (PC); inorganic phosphate (Pi); glycerophosphoethanolamine (GPE); glycerophosphocholine (GPC); phosphocreatine (PCr); adenosine triphosphate (ATP); nicotinamide adenine dinucleotides (NAD) and uridine diphospho sugar (UDP). Adapted from Lei et al. of Reference 24. (**B**) 3D ^{17}O MRSI of natural abundance H_2 ^{17}O (*top row*) and corresponding ^{1}H anatomical images (*bottom row*) of rat brain acquired at 9.4T. The ^{17}O surface RF coil positions and cross sections are indicated in the images.

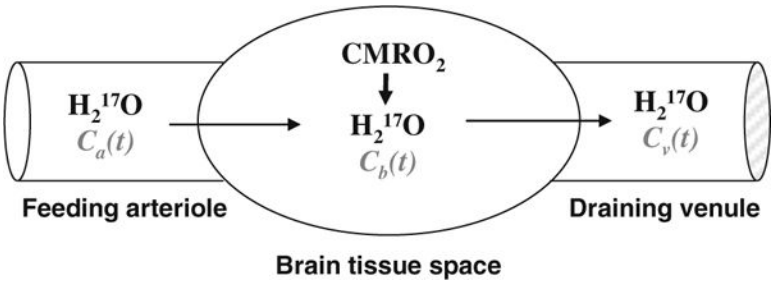

Fig. 15.3.

Schematic illustration of a "complete model" describing three parallel processes of the ^{17}O -labeled metabolic water ($H_2\ ^{17}O$) occurring in the brain when the ^{17}O-labeled oxygen gas molecules are introduced via an inhalation. In this model, only the metabolic $H_2\ ^{17}O$ is considered because the ^{17}O-labeled O_2 is invisible by in vivo ^{17}O NMR. *Ca(t)*, *Cb(t)* and *Cv(t)* stand for the $H_2\ ^{17}O$ concentration in arteriole, brain tissue and venule, respectively, as a function of the $^{17}O_2$ inhalation time.

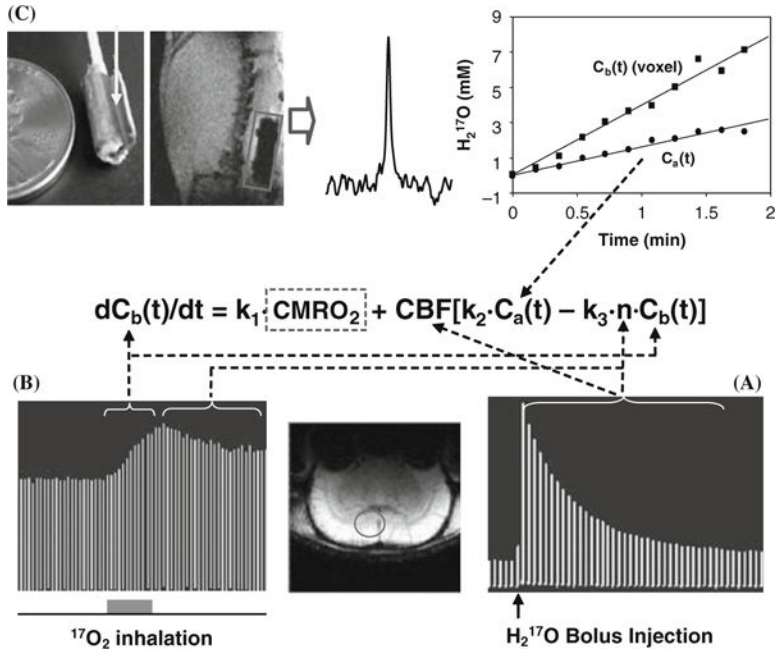

Fig. 15.4.

Schematic diagram showing the multiple in vivo ^{17}O measurements for determining $CMRO_2$ using the complete model according to the mass balance equation of Equation (15.8) which links Cb*(t)*, Ca*(t)*, CBF and *n* with $CMRO_2$. To simplify the equation, three known constants of $2\alpha_1$, mf_2 and m/λ used in Equation (15.8) are replaced by k1, k2 and k3, respectively. (A) Stacked plot of the ^{17}O spectra of cerebral $H_2{}^{17}O$ tracer from one representative rat brain voxel as indicated by the circle in the anatomical image (*low center insert*). The spectra were acquired before and after a bolus injection of $H_2{}^{17}O$ for CBF measurements. (**B**) Stacked plot of the ^{17}O spectra of the metabolic $H_2{}^{17}O$ from the same representative voxel acquired before (natural abundance), during (as indicated by the *gray bar under the stacked plot*) and after a two-minute $^{17}O_2$ inhalation. (**C**) Measurement of Ca*(t)* by using an implanted ^{17}O RF coil (*the left insert*). The middle insert illustrates a ^{17}O spectrum of natural abundance $H_2{}^{17}O$ obtained from the rat carotid artery blood by using the implanted RF coil before $H_2{}^{17}O$ inhalation. The right insert shows the time course of Ca*(t)* (*circle symbol*) and Cb*(t)* from a representative 3D ^{17}O CSI voxel (*square symbol*) in the same rat during a two-minute inhalation of $^{17}O_2$. Finally, the ratio between the ^{17}O signal decay detected after a bolus injection of $H_2{}^{17}O$ (see Fig. 15.4A) versus the ^{17}O signal decay detected after the cessation of $^{17}O_2$ inhalation (see Fig. 15.4B) gives the constant of *n*. Adapted from Zhu et al. of Ref (54).

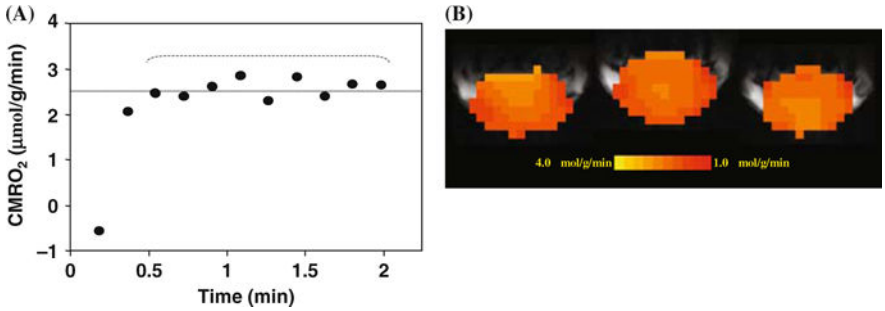

Fig. 15.5.

(**A**) Plot of the calculated $CMRO_2$ values using the complete model as described by Equation (15.9) as a function of $^{17}O_2$ inhalation time. (**B**) Three-dimensional coronal $CMRO_2$ images of rat brain measured by in vivo ^{17}O MRS approach during a two-minute $^{17}O_2$ inhalation. Adapted from Zhu et al of Ref. (s). (*See* Color Plate)

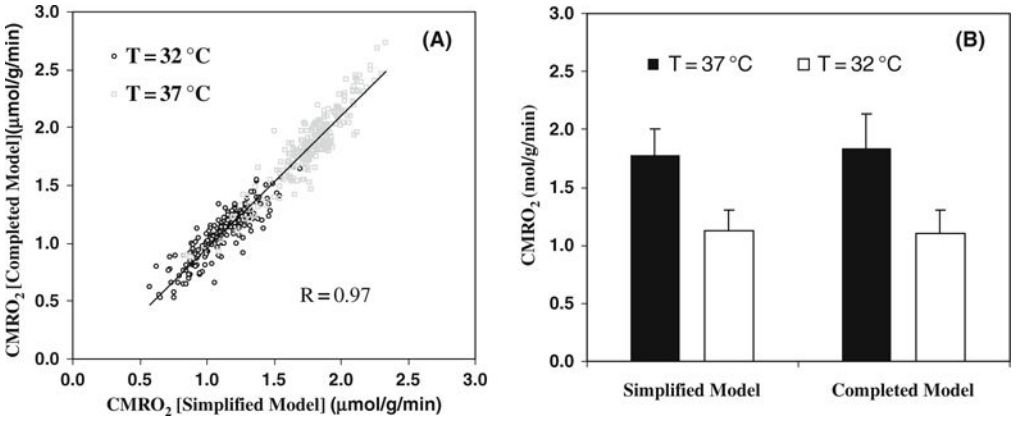

Fig. 15.6.

(**A**) Voxel based $CMRO_2$ calculation and comparison using the completed and simplified models from a representative rat (total voxel number used was 224 for 32°C and 254 for 37°C, voxel size = 75µ). (**B**) Averaged $CMRO_2$ values in the same rat brain at normothermia (37°C) and hypothermia (32°C) conditions, calculated with simplified and completed model, respectively. Adapted from Zhu et al of Ref. (86).

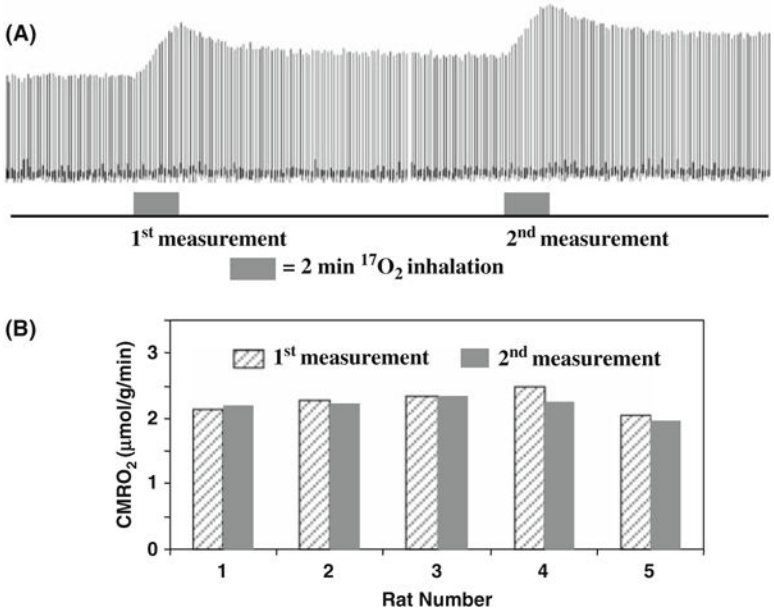

Fig. 15.7.

(**A**) Stacked plots of $H_2{}^{17}O$ spectra from a representative voxel of 3D ^{17}O MRSI data acquired before, during and after two consecutive two-min $^{17}O_2$ inhalations in a rat brain. (**B**) The comparison results between two repeated $CMRO_2$ measurements in five rat brains. Adapted from Zhu et al of Ref. (86).

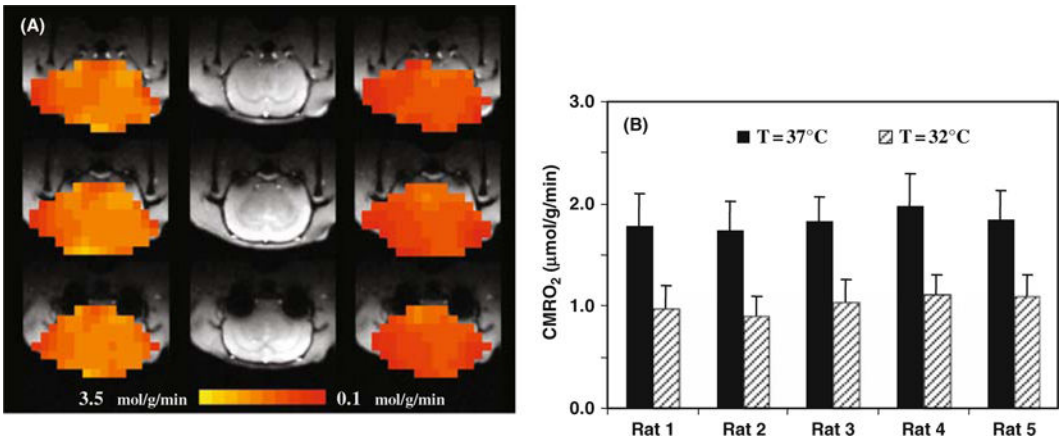

Fig. 15.8.

(**A**) 3D $CMRO_2$ maps of a representative rat brain obtained at normothermia (*left column*) and hypothermia (*right column*), and their corresponding anatomic images (*middle column*). (**B**) Summary of $CMRO_2$ results measured at normothermia and hypothermia conditions (n = 5). Adapted from Zhu et al of Ref. (86). (*See* Color Plate)

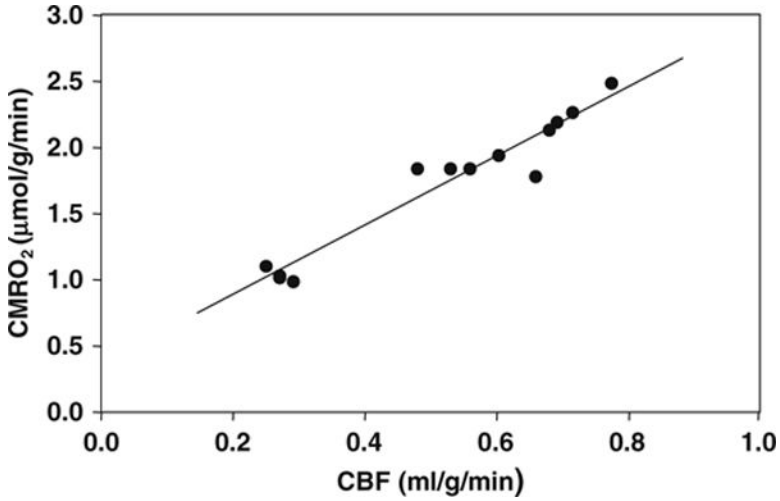

Fig. 15.9.

Correlation of CBF and $CMRO_2$ values in the rat brains anesthetized with α-chloralose at brain temperature range of 32–37°C. The linear correlation coefficient (R) was 0.97. Adapted from Zhu et al. of Ref. (86).

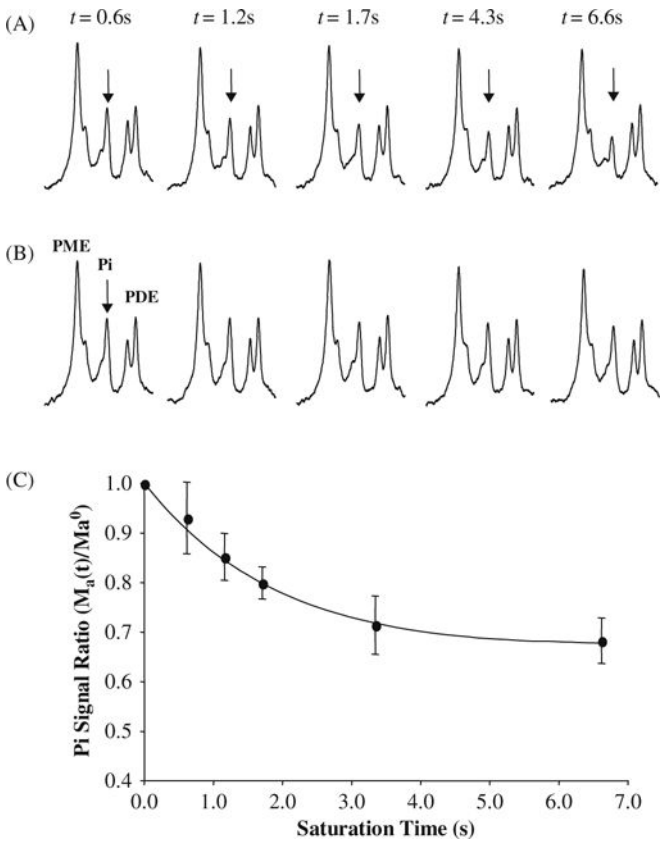

Fig. 15.10.

(**A**) Progressive saturation measurements and averaged in vivo ^{31}P spectra (partially displayed) as a function of γ-ATP saturation time (*t*), and (**B**) their corresponding control ^{31}P spectra. The arrows point to the Pi resonance peak. (**C**) Normalized Pi signal change as a function of *t* and regression fitting (*solid line*) according to Eq. (15.13a). Adapted from Lei et al. of Ref. (20).

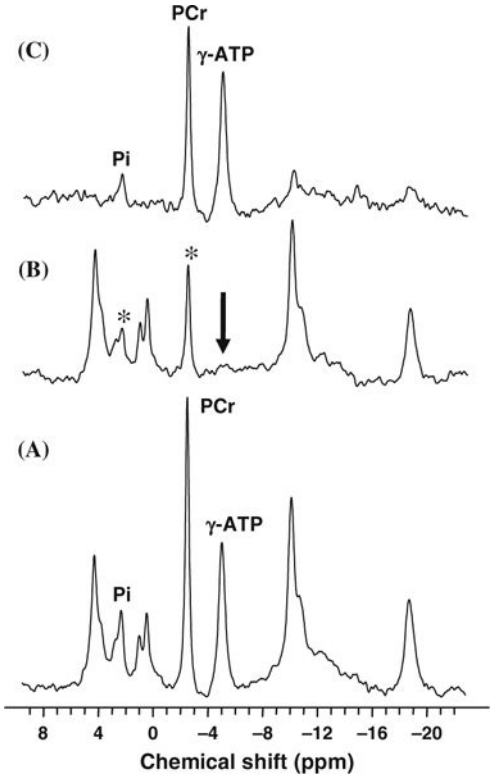

Fig. 15.11.

In vivo ^{31}P spectra acquired from a health human occipital lobe in the absence (**A**) and presence (**B**) of complete γ-ATP saturation, and the difference spectrum (**C**) between the two. Only the Pi and PCr resonance peaks show the magnetization transfer effect due to the saturation. The intensity reduction of Pi can be used to determine the forward rate constant and flux for the ATPase reaction, and the intensity reduction of PCr can be used to determine the forward rate constant and flux for the CK reaction. Adapted from Lei et al. of Ref. (20).

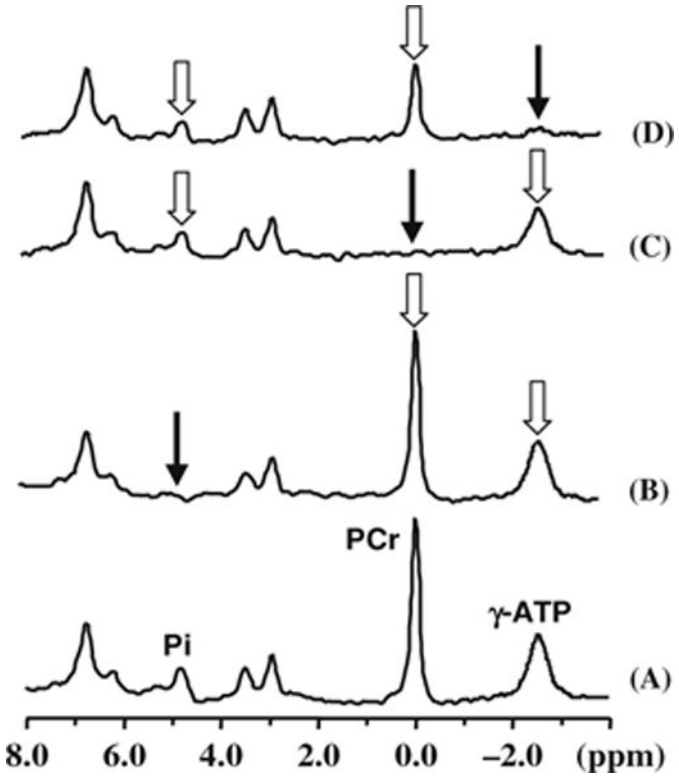

Fig. 15.12.

In vivo ^{31}P MSS MT measurements and four spectra acquired from a representative human occipital lobe in the absence (**A**) and presence of complete RF saturation on the resonance peak of (**B**) Pi (Step 2), (C) PCr (Step 3) and (D) γ-ATP (Step 1), respectively. The narrow arrows indicate the saturation sites and the wide arrows indicate the signal reductions due to the magnetization transfer. Adapted from Du et al. of Ref. (50).

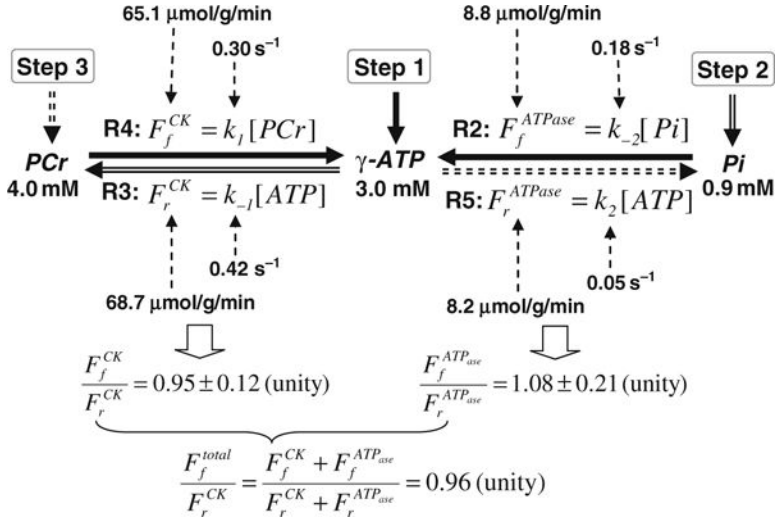

Fig. 15.13.

Chart showing the three-step measurements of in vivo ^{31}P MSS MT approach for determining the entire ATP kinetic network and associated metabolic rate constants and fluxes, and the measurement results from the human occipital lobe. Step 1 measures two forward reactions (**R2** and **R4**) along the solid arrows. Step 2 measures the indirectly coupled reverse reaction (**R3**) along the double-line arrows. Step 3 measures another reverse reaction (**R5**) along the dotted-line arrows. All results point to the fact that flux ratios satisfy the chemical equilibrium condition.